

COST CA 19111

European Network on Future Generation Optical Wireless Communication Technologies (NEWFOCUS)

Deliverable D3.1

Transceiver designs for VLC solutions, as well as advanced PHY solutions for FSO links

Date: 27/04/2023

Edited By:

Beatriz Ortega (Universitat Politecnica de Valencia, Spain)

Stanislav Zvanovec (Czech Technical University in Prague, Czech Republic)

List of contributors

Name	Country
Stanislav Zvanovec	CZ
Beatriz Ortega	ES
Jan Bohata	CZ
Zabih Ghassemlooy	UK
Zun Htay	UK
Xiaodan Pang	SE
Vicente Matus	ES
Rafael Perez-Jimenez	ES

1. Introduction

The continuous growth of the number of smartphones, wearables, tablets or internet of things devices, and the emerging of new multimedia services, such as cloud access, 4K/8K high definition video, augmented virtual reality, online gaming or social networking, exceeds the capabilities of the current mobile network. As expected [1], there will be 5.3 billion total internet users (66% of the global population) by the end of 2023, the number of mobile devices will increase up to 13.1 billion and 1.4 billion of these will be 5G. Moreover, the evolution of the legacy mobile communication networks up to 5G and beyond will enable downlink experience user over 1Gb/s, 30 bps/Hz spectral efficiency, latency lower than 1 ms, connection density of 1,000,000 device/km² and high efficient power consumption [2].

Due to the congestion of lower microwave bands employed in conventional cellular services, a number of emerging technologies will be required to provide technical solutions for wireless communications, namely free space optics (FSO) and visible light communications (VLC). This deliverable aims to present the recent advances in transceiver solutions proposed for such systems by several collaborations between research groups from different partners in COST action CA19111 NEWFOCUS.

2. State of the art

2.1. MIMO FSO systems

In FSO systems, link availability becomes a major issue due to its peculiar characteristic of being susceptible to atmospheric conditions [3]. Fog and turbulence contribute the most to the degradation in the link performance by way of both amplitude (power) and phase fluctuation of the optical wavefront while propagating through the free space channel. To address the weather impact on the FSO link performance and ensure link availability at all times, techniques such as hybrid RF/FSO, multiple input multiple output (MIMO) FSO with spatial diversity (SD), and relayed FSO systems have been proposed in the literature [3]. Amongst the proposed solutions, SD techniques has been proven to perform better compared to the single FSO link in terms of bit error rate (BER) performance to mitigate the degradation due to the fog condition [4].

A comparative study of single input single output (SISO) and MIMO FSO systems under different weather conditions has been reported in the literature showing that MIMO outperforms SISO in terms of the received power level and BER in [4], [5], and [6]. Aside from MIMO and SD techniques, adaptive modulation and low-density parity-check coding for the SISO FSO system were proposed in [7] showing tolerance to a deep fade of the order of 30 dB and above under strong turbulence. A novel adaptive transmission algorithm for the optimization of both power usage and spectral efficiency for the satellite to ground communications with 10 dB of power-saving was proposed in [8]. In [4], a comparative analysis of a MIMO FSO link with adaptive switching to ensure link availability and SISO FSO under fog and turbulence conditions together with the investigation of the optimal threshold in terms of bit error rate (BER) in a GNU Radio platform was reported. The analysis of adaptive modulation FSO system with multi aperture using signal to noise ratio (SNR) threshold for dynamic adaptation of the modulation scheme was also reported in [9].

While there is a large body of literature on theoretical and simulation-based analysis on the optimization of FSO systems using adaptive algorithms, very little has been reported on the practical implementation of such systems. Most reported works in the literature are purely based on hardware solutions involving the use of traditional optical sources, photodetectors (PDs), and integrated circuit boards, which limit cross functionality and can only be modified through physical intervention. Even though there is a reconfigurable hardware solution involving the use of field programmable gate arrays (FPGAs) or digital signal processing (DSP) boards, it requires highly skilled and specialized personnel [10], [11]. It is worth mentioning that software defined radio (SDR)-based platforms have been known to provide flexibility and reconfigurability in practical implementation and evaluation of adaptive techniques in MIMO FSO systems. Additionally, SDR, which is designed to remove hardware limitations, offer many advantages including (i) implementation of signal processing through the physical and medium access control layers [12]; (ii) software-configurability and control; (iii) improved system performance with the efficient and flexible use of the RF spectrum for new services to the end users; (iv) a reduced system size and minimization of the design risk and time-to-market; and (v) flexibility in research and development due to the implementation and verification of a range of newly developed protocols [13]. The experimental implementation of SDR based RF systems utilizing universal software radio peripheral (USRP) were reported in [14], [15] and, [16]. Highly flexible and powerful SDR platforms to accommodate 5G wireless networks have been reported in the literature [17] for the virtualization of SDR and SDN.

Although the SDR implementation of RF systems is rather common and well-established, in OWC, we have also found some work on system implementation using various available software defined platforms including MATLAB, LabVIEW, GNU Radio, etc. for DSP and controlling the hardware. Experimental demonstration of a bi-directional visible light communication (VLC) system with adaptive modulation based on the noise, interference, and environmental impacts was proposed and investigated [18]. In [10], experimental evaluation and performance analysis of a VLC system were carried out using USRPs and LABVIEW software for audio streaming over a 1 m linkspan. Adaptive VLC system with adaptive software defined equalization techniques such as least mean squares, normalized least mean squares, and QR decomposition-based RLS (QR-RLS) were analyzed in [19]. In [20], a commercially available OWC test kit (for both visible and infrared (IR) bands) with an SDR platform (i.e., compatible with LimeSDR USB and GNU Radio) for use in indoor, outdoor and underwater communication applications with a transmission range over 20 m have been reported. Design and demonstration of the IR optical front end with a bandwidth of 10 MHz with USRPs was reported in [21], which was validated by the transmission of an audio signal. In [22], the advantages of implementing FSO systems based on SDR under different weather conditions to increase the link availability and reliability were investigated. The reported works in the literature mainly utilized the LabVIEW software as the SDR ecosystem for control, test, and deployment of the system in real-time. Alternatively, GNU Radio, which is a free and open-source software development toolkit, supports the real time emulation to control and deploy the hardware using the time domain graphical user interface (GUI) [23]. We have reported the performance analysis of SDR based MIMO and SISO FSO systems under different fog and turbulence conditions with adaptive switching in GNU Radio in [4].

2.2. VLC OCC systems

Optical Camera Communications (OCC) is a growing sub-field of VLC that aims to provide low-speed downlinks from LED-based transmitters to cameras [24] [25]. VLC systems re-utilize the

existing illumination infrastructure to transmit data through modulated light signals, and, in turn, OCC systems leverage the widely-available camera equipment to implement receivers. The camera acquires the transmitted signal by capturing video and decoding it with image processing software. Most OCC systems in literature can be divided into two main categories: those that use the rolling shutter (RS) effect of cameras, in which each row (or column) of pixels is exposed sequentially, or those that use global shutter (GS), where all pixels are exposed simultaneously. For photographic purposes, RS detracts the picture quality, especially in high-movement scenarios. Nevertheless, this is the most popular type of camera in electronics nowadays since sequential scanning allows the reuse of whole blocks of circuitry, making RS-based cameras less costly. Furthermore, for communication purposes, the RS acquisition allows capturing different states of the VLC transmitter in one single image frame, allowing it to multiply the achievable data rate, which in turn, in GS, is upper bounded by the frame rate of the camera in fps. Different processing techniques have been developed depending on the nature of the camera, whether it uses GS or RS image sensor. However, it is worth mentioning that the GS processing approach can be applied when using RS hardware. The RS-based OCC is one of the most popular techniques due to its higher data rate of several kbps compared to tens of bps in GS.

Various applications of VLC and especially OCC have been extensively developed for indoor environments, where existing lighting infrastructure and moderated background light, paired with short link distances, make communication feasible, yet, for the outdoors, photodiode-based VLC systems fail because of high-intensity background light coming from the sun and other surfaces reflecting it. On the other hand, the image-forming optics of cameras allow the segregation of the light coming from VLC transmitters efficiently, making OCC an obvious candidate for long-range outdoor systems. Moreover, several millions of photosensitive pixels form the camera's image sensor, allowing it to receive information from multiple sources simultaneously. Long-range outdoor OCC can be used for applications such as vehicle-to-vehicle (V2V) and vehicle-to-infrastructure (V2I) communication and for wireless sensor networks, making use of the growing deployment of car dashcams and the ever-increasing number of surveillance cameras. The image-forming optics of cameras allow the segregation of the light coming from VLC transmitters efficiently, making OCC an obvious candidate for long-range outdoor systems. Moreover, several millions of photosensitive pixels form the camera's image sensor, allowing it to receive information from multiple sources simultaneously. Long-range outdoor OCC can be used for applications such as vehicle-to-vehicle (V2V) and vehicle-to-infrastructure (V2I) communication and for wireless sensor networks, making use of the growing deployment of car dashcams and the ever-increasing number of surveillance cameras. In long-range scenarios, the RS systems mentioned above are bound to use extensive light sources at the transmitter pair with large optics at the receiver, i.e., several hundred millimeters lenses to capture as many rows of pixels as possible. However, the physical size of RS Tx and Rx in long distances is impractical because it leads to a reduced field of view, with a significant portion of the image dedicated to communication and no support for re-utilizing existing camera hardware. In turn, sub-pixel systems have been developed in [26-28] using GS demodulation techniques, small Tx and Rx optical front-ends, and achieved link distances above a hundred meters. The term sub-pixel stands for the case

when the geometrical projection of the Tx over the image sensor is under the area of a single pixel.

2.3. Millimeter wave signals over FSO

With the incredible growth of the number of consumer wireless devices in use, the 5G incorporates the millimeter wave (mmW) frequencies bands (30 to 300 GHz), as a main enabling technology, that will assist in achieving the high data rate and increased available bandwidth of cellular systems [29, 30]. The lower-frequency spectrum adjacent to 4G bands would provide an easier transition to 5G due to component maturity and the nature of the signal propagation characteristics. However, it is not a viable option mainly due two reasons. First, the sub-6 GHz spectrum has already been very crowded, filled with distributed bands dedicated to cellular communications, satellite and aerial communications, and wireless local area networks (WLANs). Secondly, mmW frequencies exhibits an enormous available frequency spectrum.

The latest mobile standard, 5G NR, supports sub-6 GHz frequency range 1 (FR) [31] and mmW frequencies bands between 24.25 and 52.6 GHz (FR2) [32]. According to [32], *Table 2.3.1* specifies FR2 frequency bands and the channel bandwidths of the 5G NR standard. Many countries have released a number of mmWave bands for 5G NR communications in the K-band (European countries or China), Ka-band (European countries, USA or Japan) and V-band (European countries, USA or China).

Table 2.3.1. NR operating bands in FR2.

Band	Frequencies (GHz)	Common name	Bandwidth (MHz)
n257	26.50 – 29.50	Ka-band	50 – 400
n258	24.25 – 27.50	K-band	
n259	39.50 - 43.50	V-band	
n260	37.00 – 40.00	Ka-band	
n261	27.50 – 28.35	Ka-band	
n262	47.20 – 48.20	V-band	

Besides its huge available bandwidth, i.e. 270 GHz, mmW bands have several benefits compared with the existing wireless technologies [29,30,33]. Owing to short wavelengths, the component size can be reduced which enables large antenna arrays with small physical dimension. With the same antenna size, more antenna elements can be packed at mmW frequencies than at microwave bands and, then, the formed beam can be narrower which may be employed in other applications like radar detection. Furthermore, mmW signals enable to work with small-cell networks and frequency re-use is allowed due to low interferences, i.e. short wavelength and highly directional beams; and propagation characteristics, i.e. short range. Finally, there is still unlicensed mmW spectrum (Release 17, 5G NR-U)[34], i.e. 57 to 71 GHz, for various communication applications, e.g. Industry 4.0 and internal information technology infrastructure [35].

However, mmW signals present several challenges in terms of electronic circuit design and propagation [33]. On the one hand, mmW signals are susceptible to non-linear distortion produced by electrical amplifiers due to hardware manufacturing imperfections. Besides, phase noise is another

huge challenge in the design of electronic components, which degrades severely the signal and poses great dare to mmW communications due to high oscillation frequency. On the other hand, the physical obstacles in real applications will weaken the mmW signals reducing the transmission range since its poor diffraction. Moreover, in terms of attenuation, mmW signals are affected by atmospheric gases, free space losses and weather fading.

From the network perspective, existing optical fibers and also free space optics (FSO) links allow to provide fixed/mobile convergence with sufficient bandwidth to deliver high-speed services over long distances with low cost, high reliability and low latency [36].

Therefore, in cloud-radio access network (C-RAN) networks, the availability and costs of the optical infrastructure become critical, especially in the small-cell environment [37]. As it is well known, the C-RAN architecture hosts the baseband units (BBUs) at the central office (CO) separated from the remote radio heads (RRH). This is enabled by optical fronthaul network connecting the RRHs with the centralized BBU pool. A backhaul segment is also defined between the BBUs and the gateway interface to the transport network. Therefore, RRHs are simplified since medium access control (MAC) layer functions, digital-to-analog and analog-to-digital conversion (DAC/ADC), radio frequency (RF) frontends and baseband processing are held in the BBUs located at the CO [37]. The BBU pool in this scenario includes an array of directly modulated lasers (DMLs) emitting at different wavelengths which are multiplexed for downlink transmission [38]. At the hotspot site, after channel demultiplexing, the optical receiver in each RRH performs the opto-electronic conversion and further amplification. C-RAN also supports open platform and real-time virtualization technologies to provide dynamic shared resource allocation in the BBU pool, in addition to multi-vendor and native support to collaborative multipoint (CoMP) radio technologies due to the very low latency between BBUs hosted at the same pool. Broad coverage can be provided due to a large number of remote RRHs connected to a centralized BBU pool with a span fiber link, typically up to 10 km for 5G or 20 km for 4G (LTE/LTE-A) [39].

A solution for the use of digital fiber optic interfaces in the 5G fronthaul network based on enhanced common public radio interface (eCPRI) has been recently proposed [40], although more complex RRHs and high bandwidth connections are required regardless of the architectural choice used for splitting the protocol functions [41,42]. However, analog-radio-over-fiber (A-RoF) solutions are very promising for cost-efficient, low latency and large bandwidth links [43]. In the RoF scheme, mmW signals can be transmitted either using RF or an intermediate frequency (IF) over optical fiber. In the former one, the CO directly transmits the mmW signal, modulated into the optical domain, over fiber fronthaul network to the RRH without the need for frequency up-conversion at the RRH side. However, high speed photodetectors and optical transmitters are required and, moreover, fiber chromatic dispersion has a significant impact on the link performance for high frequencies. On the contrary, the latter technique allows transportation of multiple aggregated IF modulated bands e.g., in low speed DMLs, and the up-conversion is held at the RRH just before wireless transmission. The use of lower speed optoelectronic devices and reduced impact of fiber chromatic dispersion are the main advantages compared to a classic RoF approach, although the complexity and costs of RRHs are increased with the need for mmW local oscillator and high speed mixers. However, mmW local oscillator delivery at the RRH has been demonstrated in the literature [44,45] in order to provide flexibility in such systems and multiple IF bands employing OFDM formats have been transmitted up to several Gb/s bitrate [46].

However, in a centralized architecture, mmW signal generation based on photonics [47,48] may be located at the BBU in the CO as part of the shared hardware infrastructure although other schemes

can be adopted to mitigate signal degradation for certain signals and network conditions since IF signal would be transmitted over fiber and the photonic up-conversion would be held before photodetection.

Optical transceivers based on direct and external modulation have been presented in the previous literature. External data modulation presents some benefits due to the use of large bandwidth dual drive Mach-Zehnder modulators (MZM) with zero chirp to reduce the impact of fiber dispersion. Although the operating bias point of MZM undergoes voltage drift and insertion losses should be compensated by an EDFA or increasing the laser optical power, intensive research has been recently conducted towards improving the maximum bitrate that can be achieved [49]. Moreover, external modulators are expensive, besides polarization independence, good linearity and smaller size characteristics which are also required. DMLs are potentially more suitable than externally modulated transmitters for 5G networks. Previous works have successfully demonstrated the use of DMLs for signal transmission, e.g. a 112 Gbit/s dual-polarization 16-QAM signal using a 35 GHz DML [50] or 28-Gbaud PAM-4 and 56-Gbit/s non-return-to-zero (NRZ) signals employing a 30 GHz DML at 1310 nm [51].

3. Recent achievements in outdoor transceivers

3.1. Transceivers for FSO

Two atmospheric transmission windows at the mid-wave IR (MWIR, 3-5 μm , 60-100 THz) and the long-wave IR (LWIR, 8-12 μm , 25-37 THz) in the mid-infrared (MIR) region (wavelength range of 3-50 μm) contain a rich potential for FSO technologies and communication purposes, yet to be exploited. Compared with the MMW and sub-THz bands being heavily studied and discussed for 6G wireless communications, the MWIR and LWIR have almost two orders of magnitude lower atmospheric propagation attenuation with a tenfold broader fully unlicensed bandwidth [52]. On the other hand, compared with the 1.5- μm telecom band in the short-wave IR (SWIR, 1-2.5 μm), where most commercial FSO communications are developed, the MWIR and LWIR have much higher resilience against adverse weather, e.g., much lower sensitivity to particle scattering atmospheric turbulence effects [53]. Moreover, the mid-IR region shows a lower risk for eye safety [54]. An often-adopted approach to carrying out mid-IR FSO system demonstrations is using wavelength conversions. However, the high-power consumption associated with the nonlinear wavelength conversion in such methods leads to energy deficiency and hardware complexity, obstructing practical development. A more attractive choice in the long-term would be direct-emission semiconductor lasers and photodetectors. Quantum cascade devices, including quantum cascade lasers (QCLs), are based on inter-subband transitions to cover a wide spectral range from the MIR to THz. They appear as promising candidates due to their breakthroughs in a broad bandwidth, high-temperature operation, and low energy consumption. For transceiver technologies, with the assist of QCLs, both direct modulation and external modulation schemes can be adopted.

For direct modulation, owing to the high linearity and high bandwidth characteristics of directly-modulated QCL (DM-QCL), one can use a digital-to-analog converter (DAC) to generate and modulate multi-level signals on the laser bias current.

For external modulation, one can place an external quantum Stark-effect modulator after an high-power continuous wave QCL. The modulator can also be driven by multi-level signals from the DAC.

For detection, three types of detectors with respective merits can be considered, namely, Mercury-Cadmium-Telluride (MCT) photovoltaic detectors, quantum cascade detectors (QCD) and quantum-well infrared detectors (QWIP). MCT detectors are often thermoelectric-cooled to ~ 200 Kelvin to ensure a satisfactory noise performance. Moreover, the bandwidth of MCT detectors is also often limited to sub-GHz or GHz scale. QCDs can operate at room temperature without any bias or active cooling, and the bandwidth of QCDs are also normally higher than MCT, in the scale of ~ 10 GHz. However, one limitation of QCD is its responsivity, normally requiring high incident power with accurate focus and small spot size, which impose high requirements on collimation and focusing of the lenses. Finally, QWIPs are normally operated with a bias voltage. It can also work at room temperature without cooling or temperature control. Moreover, up to 70 GHz bandwidth QWIP has been demonstrated and reported recently, making it a promising candidate for practical applications. However, one critical drawback of QWIP is its high noise level, often hindering the transmission of multilevel signals.

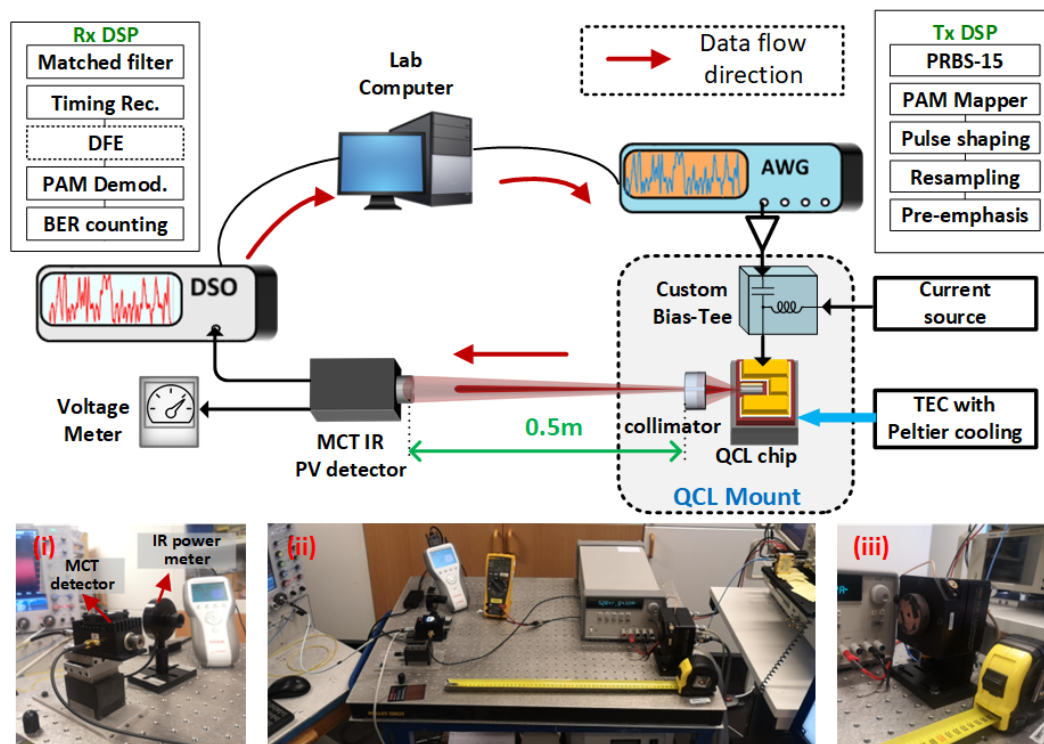


Figure 3.1.1. Experimental setup of MWIR DM-QCL- and MCT detector-based FSO transceiver characterization.

A few lately demonstrated MIR FSO systems in both MWIR and LWIR bands have been reported. QCLs are employed for directly modulation and Stark-effect modulator is employed for external modulation. The purpose of these system-level studies is to evaluate the large-signal characteristics of the MWIR/LWIR transceivers. As shown in Fig. 3.1.1, The first demonstration employed a fabricated MWIR QCL chip [55], which a distributed feedback (DFB) laser module with a center wavelength of $4.65\text{-}\mu\text{m}$. The laser chip and the bias tee are mounted on a commercial QCL mount (ILX Lightwave LDM-4872) with a Peltier temperature controller (TEC) and a water-cooled base. A beam collimating lens installed at the QCL mount is used to collimate the high-divergence optical beam emitted from the QCL chip. The highly directive mid-IR signal is transmitted over a 0.5-m distance, which is chosen due to the tabletop space constraint and local laser safety regulations. At the receiver, we firstly calibrate the

received signal power with an IR power meter. Later, we replace the IR power meter with a commercial MCT detector for the transmission measurements. The picture of the IR power meter and the MCT PD are shown in Fig. 3.1.1 (i). The PD is mounted in a thermo-electrically cooled module and has a built-in trans-impedance amplifier (TIA). The 3-dB bandwidth of the MCT PD as per the manufacture's specification is around 720 MHz. The received signal is converted to digital samples at a realtime digital storage oscilloscope (DSO) operating at 10 GSa/s. We collect the converted digital traces at the lab computer and perform a receiver-side (Rx) DSP routine offline to recover the transmitted data. The Rx DSP consists of a matched filter, timing recovery, a symbol-spaced adaptive decision-feedback equalizer (DFE), and symbol demodulation. In the end, the recovered data sequence is compared with the transmitted data for bit error rate (BER) computation. Each received signal trace consists of 520k symbols for BER calculation. We first characterize the power and frequency response of the combined QCL and MCT MIR PD subsystem. The measured P-I curve of the QCL is shown in Figure 3.1.2 (a). The QCL under CW operation has a lasing threshold of 178 mA at a temperature of 292 K (19 °C). To prevent potential damage to the QCL chip from overdriving, we measured with a laser bias current of up to 255 mA, at which the QCL has an output power of 32.7 mW. Since no sign of output saturation is observed at this power level, we keep the laser operating at this bias point during all transmission measurements. We also perform power calibration measurement of the receiver. The calibration result is shown in Figure 3.1.2 (b). Finally, we use a vector network analyzer (VNA) to characterize the end-to-end frequency response of the system from the QCL input to the MCT PD output. During the measurements, we observe that the system bandwidth is correlated with the laser power, and increasing the power beyond an optimal value causes a decrease in bandwidth. Such a bandwidth-power correlation may be attributed to the known fact that the QCL modulation bandwidth often varies with the laser bias or further partly due to the detector saturation. In our configuration, the optimal received optical power (ROP) is found to be 10 mW, corresponding to a detector PV of 1.3 V. Figure 3.1.2 (c) shows the characterized system bandwidth at the optimum received power level. The end-to-end 3-dB bandwidth is found to be around 320 MHz, and 6-dB bandwidth is around 450 MHz. The current system bandwidth is most likely limited by the MCT MIR PD and the electrical parasitic in the laser mount.

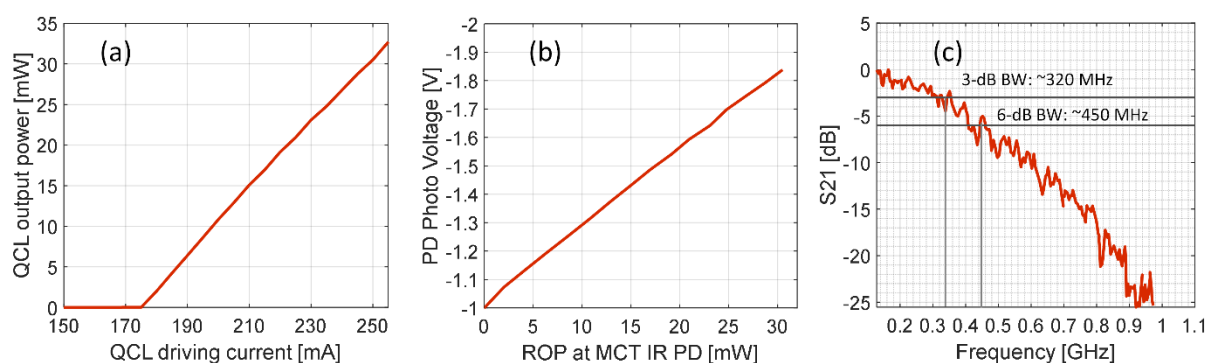


Figure 3.1.2. (a) The output power of the QCL under CW operation as a function of driving current; (b) The MCT IR PD PV as a function of the received optical power (ROP); (c) End-to-end S21 characteristics measured at optimum received optical power level.

Finally, large signal analyses were performed with both binary signal, i.e., non-return-to zero (NRZ) and multi-level signals, i.e., pulse amplitude modulation (PAM). The maximum data rate achieved below

the 6.7%-overhead (OH) staircase hard-decision (HD)-forward error correction code (FEC) limit of $4.5E-3$ is 6 Gbps with PAM-8. The eye diagrams of different transmitted signals are shown in Fig. 3.1.3.

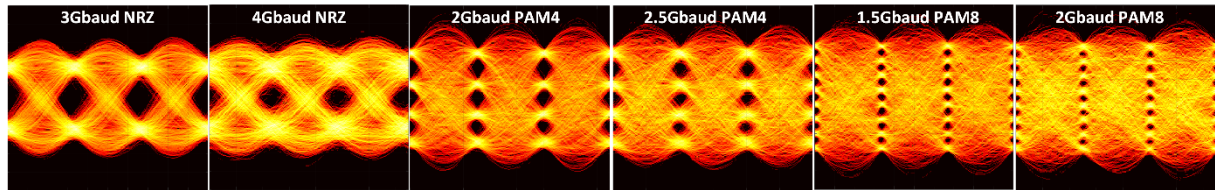


Figure 3.1.3. Selected eye diagrams of the received signal after the MWIR DM-QCL and MCT-based FSO link.

Then we use a similar testbed and study a LWIR DM-QCL-based transmitter and a QCD-based receiver [56]. The DM-QCL used in our experiment is a 3-mm DFB ridge laser fabricated epi-down. In this way, the laser chip can be operated at room temperature with the help of a Peltier thermoelectric controller (TEC). The laser chip was soldered on a sub-mount and then wire bonded to a high-frequency coplanar waveguide. Fig. 3.1.4 (a) shows the picture of the QCL mount and the zoomed view of the DFB-QCL chip. The output of the DM-QCL is a continuous wave centered at a wavelength of $9.6 \mu\text{m}$ with a few tens of milliwatts of output power. The device has a cut-off modulation frequency of around 3 GHz, beyond which the frequency response drops drastically. In our transmission system experiment, we use a Peltier TEC to stabilize the DM-QCL operation temperature at three different points, i.e., 10°C , 5°C , and 0°C . Fig. 3.1.4. (b) shows the characterized L-I-V curve of the laser at the selected operating temperature values. One can observe that the DM QCL starts lasing around 560 mA injection current at all investigated temperatures and saturates at around 675 mA.

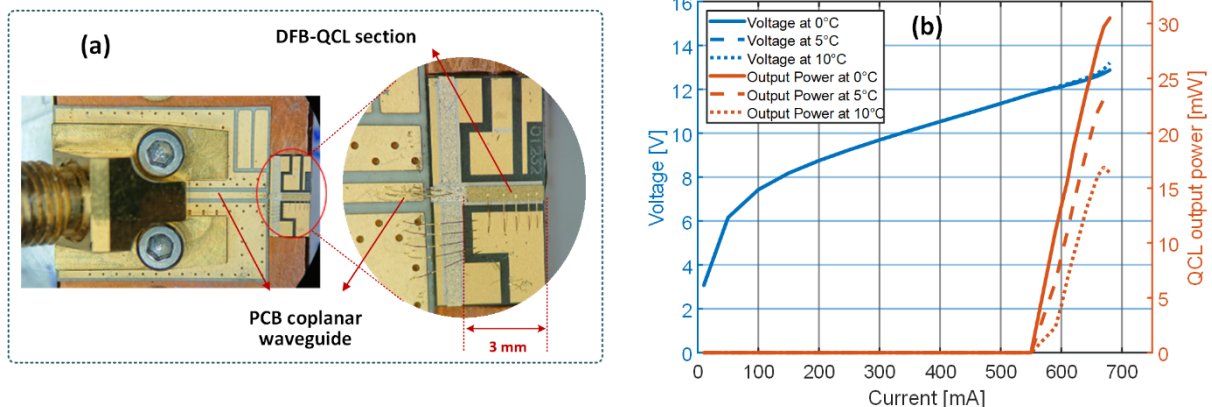


Figure 3.1.4. (a) The PCB hosting the $9.6\text{-}\mu\text{m}$ DFB-QCL chip that is wire bonded to a coplanar waveguide delivering the bias and RF modulation signals. (b) The measured L-I-V curves of the QCL at operation temperature of 0°C , 5°C and 10°C , respectively.

The LWIR FSO receiver for this experiment is a fully passive GaAs/AlGaAs QCD without any bias or cooling, operating in a room-temperature environment (no air conditioning, temperature drifting between 25°C and 30°C). Figure 3.1.5 shows the picture and the characteristics of the employed QCD. The detector was fabricated into a $55 \times 55 \mu\text{m}^2$ square mesa structure where the top contact is realized

with an air bridge. Such a mesa structure is used to operate at high frequencies, compared with traditional mesa structures with larger sizes and long wire bonds usually used for static / low-frequency measurements. The air bridge is continued by a coplanar waveguide on the GaAs substrate, which is then connected through short wire bonds to a printed circuit board (PCB) coplanar waveguide equipped with a 2.92-mm connector. The QCD is based on a diagonal transition with a 45° polished facet that satisfies the polarization requirements for optical transitions. This unipolar detector conducts in the photovoltaic regime; yet has a very wideband frequency range with a first-order roll-off. This behavior is due to the fast energy relaxation of the electrons as the only charge carriers. Also, the asymmetry of the cascade region that acts as a pseudo-electric lead to a photocurrent. The cascade region is designed in such a way that the electron relaxation lifetime from one period to the adjacent one is estimated to be shorter than 10 ps. In practice, the bandwidth is often limited by electrical parasitic capacitance in the mesa structure, packaging, and driving circuit. For this particular device, the cut-off frequency is around 6 GHz due to both the RF packaging and the impedance mismatch. Figure 3.1.5 (a) shows a picture of the QCD mount where the detector chip is wire-bonded to the coplanar waveguide. Figure 3.1.5 (b) shows the photocurrent characterization of the QCD at room temperature. The peak responsivity is measured at 141.6 meV photon energy, corresponding to 8.75 μm of wavelength. While at 9.6 μm , the detector responsivity performance drops to approximately 45%. Therefore, we can expect improved efficiency with a lightly shorter laser wavelength approaching the peak. As shown in Figure 3.1.5(c), the photocurrent of the QCD has a linear relation with the injected optical power up to 50 mW with a responsivity of 4.5 mA/W at 9 μm at room temperature. In our transmission experiment, the highest optical power measured on the detector was 30.5 mW within the linear region.

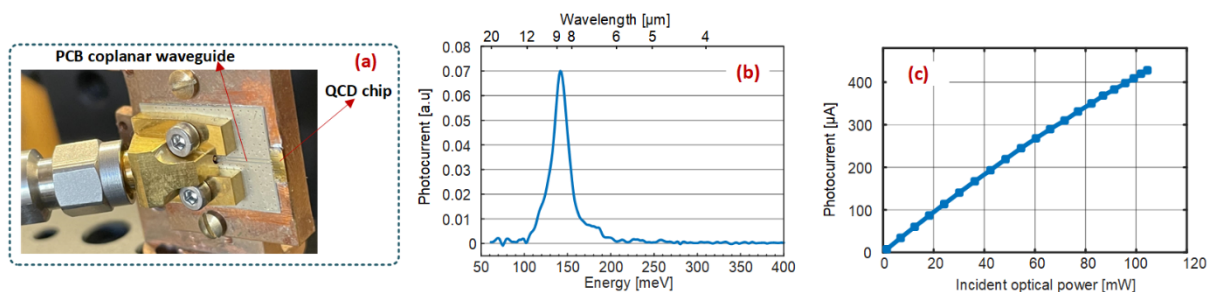


Figure 3.1.5. (a) The picture of the hosting PCB for the QCD chip. (b) The measured photocurrent spectrum of the QCD at room temperature as a function of both the photon energy and the corresponding wavelength. (c) The measured photocurrent of the uncooled QCD as a function of incident CW optical power.

Finally, large signal analyses were performed with both NRZ and PAM4. Maximum achieved data rate is 11 Gb/s with PAM4. The BER curves and selected eye diagrams at different bias point are shown in Figure 3.1.6. the trade-off between the signal SNR and modulation linearity can be clearly observed by looking at the eye diagrams, particularly in the case of PAM4. A higher coding-gain FEC configuration, 20%-OH HD-FEC, may be used for further data rate enhancement, but it is considered an unfavored option due to its increased latency and complexity.

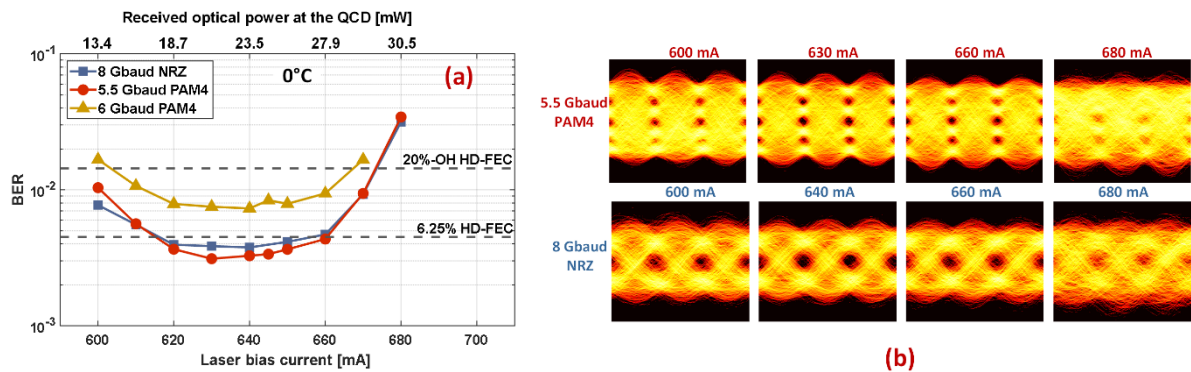


Figure 3.1.6. (a) BER as a function of the laser bias current for NRZ-OOK signal at 8 Gbaud and PAM4 signal at 5.5 Gbaud (11 Gb/s) and 6 Gbaud (12 Gb/s); (b) Selected eye diagrams for both the 5.5 Gbaud PAM4 and the 8 Gbaud NRZ-OOK signals measured at different laser bias points.

A latest demonstration was based on an external Stark-effect modulator [57]. In this demonstration, the free-space optical communication system is exclusively made of unipolar quantum optoelectronic devices. A commercial continuous-wave distributed feedback QCL is connected to a DC current source and Peltier-cooled to be operated at room-temperature (20°C). It emits 80mW at 8.6 μm wavelength, which is free-space coupled into a quantum Stark effect modulator. The external modulator is a 50 $\mu\text{m} \times 50 \mu\text{m}$ mesa with 8GHz of 3 dB-bandwidth, designed to operate at 9 μm . It can be tuned by applying a DC voltage bias (energy tuning coefficient around 5meV \cdot V⁻¹). However, a too high offset would reduce the modulation depth as it would impose a lower RF power into the device to avoid field breakdown. The output from the modulator is collimated and transmitted over a free-space link of around 70 cm. A quantum cascade detector (QCD) operating at room-temperature is placed at the end of the link as the MIR receiver. The incident beam to the QCD is carefully aligned so the output photocurrent is maximized during the measurements. The experimental configuration is shown in Figure 3.1.7.

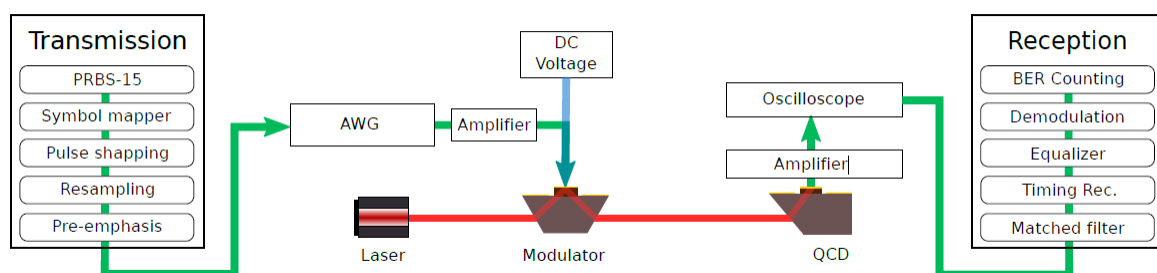


Figure 3.1.7. Schematic of the data transmission setup. A MIR quantum cascade laser emits light to an external modulator connected to a DC voltage drive and an AWG. The modulated beam is collected by a quantum cascade detector. The signal is preprocessed before being sent to the AWG and post-processed before being analyzed with a high-speed oscilloscope.

The results of system end-to-end S21 response and the large-signal transmission analyses are shown in Fig. 3.1.8. As shown in the figure, the system has a 3 dB-cutoff frequency of 2GHz. The frequency response is flat before experiencing a mild decrease (first-order roll off) with a 10 dB cutoff at 7GHz. Such a response is a specific characteristic of the intra band devices, while conventional interband

telecom devices display relaxation oscillations, generating a resonance before a second order roll off. As a consequence, for intra-band devices the maximum achievable bitrate is enhanced compared to semiconductor laser diodes with the same cutoff frequency. Figure 3.1.8 (b) shows the measured BER curves at three different bit rates after a 3-tap feedforward equalizer (FFE). The maximum achieved bit rate in this setup is 12 Gb/s. It is noted that multilevel signal formats such as PAM4 cannot achieve the same bitrate due to the limited SNR.

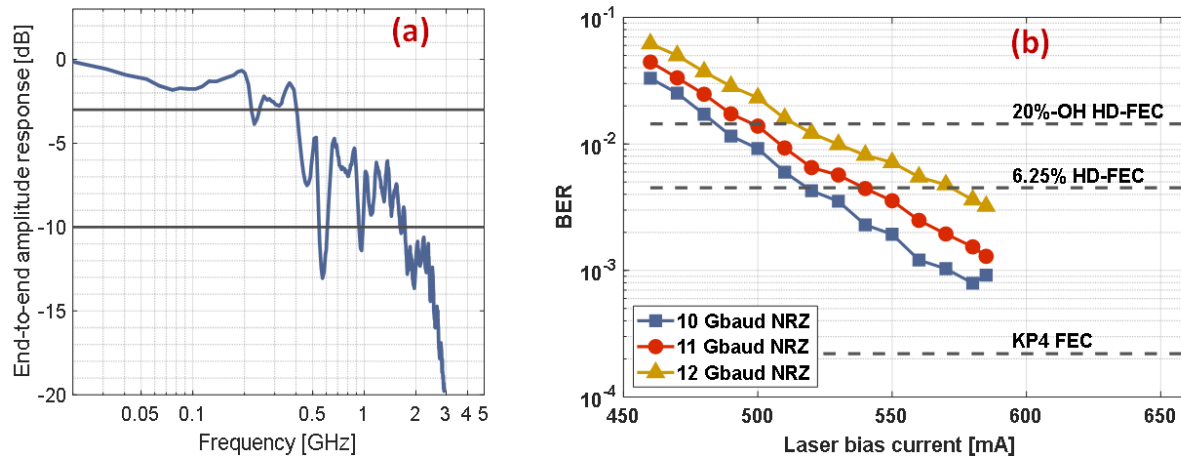


Figure 3.1.8. (a) Bandwidth characterization of the full system (AWG, modulator, detector, oscilloscope and all other electronic components). The system presents a mild frequency rolloff with a 3 dB bandwidth of 2 GHz and a 10 dB cutoff at 7 GHz. (b) BER curves for different bit rate with 3-tap FFE.

In summary, semiconductor-based solid state FSO transceivers have been underexploited in the MWIR and the LWIR region. Recent demonstrations show that the uni-polar quantum devices, including directly modulated QCLs, external Stark-effect modulators, and QCDs, have progressed fast to a maturity level for system transmissions supporting over 10 Gb/s. One can confidently extrapolate such a progress and predict over 100 Gb/s fiber-optic matching speed in upcoming years.

3.2. Transceivers for MIMO FSO

Our work adopted GNU Radio which is an open source software development ecosystem that provides digital signal processing blocks to implement the OWC and RF systems to demonstrate the MIMO FSO link availability under varying atmospheric conditions. We outlined the design and implementation of out of tree (OOT) modules/signal processing blocks integrated into GNU Radio. Then we analyze the performance of a MIMO intensity modulation-direct detection FSO system with the adaptive switching using GNU Radio under various atmospheric conditions for real-time data transmission. The proposed system with OOT modules facilitates the implementation of N number of Tx and Rx. In this work, 4x2 MIMO FSO system is considered as a proof of concept, see Fig. 3.2.1. The design employs two sets of Tx and Rx for parallel transmission of two different signals to improve link reliability.

A dedicated switching algorithm is proposed to turn on the Tx(s) based on the channel conditions. Each Tx and Rx can operate independently or in a unified cluster. Fog and turbulence-induced attenuation and geometric losses are taken into account when determining the link's reliability. Under normal weather conditions, Tx-A1 and Tx-B transmit two independent data streams. In fog or turbulence,

however, additional Tx's (Tx-A2 and Tx-B2) can be used if the following conditions, i.e., $L_{\text{Atm}}(\text{input}) \geq L_{\text{Atm}}(\text{Thres})$ or $\sigma_I^2(\text{input}) \geq \sigma_I^2(\text{Thres})$ are met. This is to ensure that the link's availability is maintained to the maximum extent possible at the expense of increased transmit power P_{Tx} . On the Rx side, the received optical beams are focused by optical collimators onto two optical Rx's (Rx-A and Rx-B), which are composed of PD and trans-impedance amplifiers. The electrical signal that has been regenerated is then applied to moving average filters, samplers, and threshold detectors (slicers) to recover the estimated sequence of the transmitted data stream. The BERT is then employed to determine the real-time BER by comparing the received and transmitted data streams. Note that (i) the used parameters and link characteristics in terms of the channel loss (V , σ_I^2 , and C_n^2) are monitored using SDR/GNU Radio, and (ii) the extracted link characteristics and the received OOK signal are generated in the GNU Radio software domain. In this research, it is assumed that the signals transmitted and received are uncorrelated [58]. Based on the numerical evaluation of L_{Atm} for a given V and L , the link status is studied and a set of Tx's to be used is carried out. Note, σ_I^2 and C_n^2 are predicted to reach a forward error correction (FEC) BER of 3.8×10^{-3} , the upper limit.

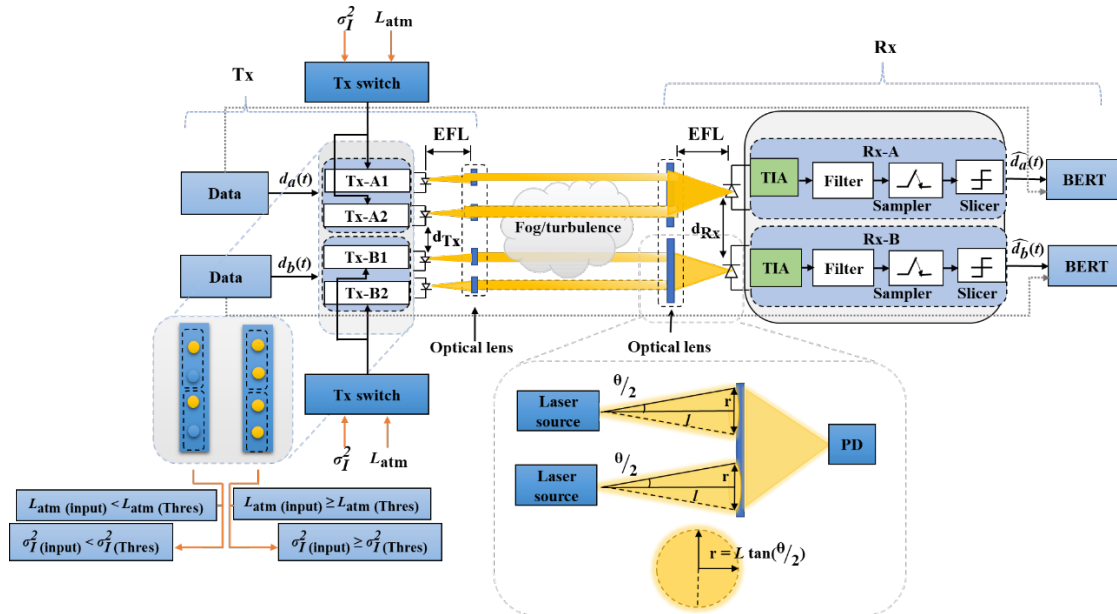


Fig. 3.2.1. Schematic system block diagram of MIMO FSO system with adaptive switching algorithm in software defined GNURadio ecosystem.

In this simulation, single FSO, MIMO FSO, and proposed MIMO FSO links with a range of 100, 200, and 300 m under turbulence and fog conditions are considered. The information on CSI (i.e., σ_I^2 and L_{Atm}) is already available at the Tx unit or provided via a feedback path. To investigate the performance of the software defined adaptive switching MIMO FSO system, the SDR-based Tx, Rx, and channel have been implemented in GNURadio, along with a general-purpose processor-based real-time signal processing framework. The GNURadio is also capable of functioning as a simulation environment without the need for actual hardware. Note that GNURadio applications are typically written in Python as a package and combined with DSP blocks integrated within GNU Radio and implemented in C++ to perform crucial signal processing tasks [59]. Fig. 3.2.2 depicts the implementation of the MIMO FSO system in the GNU Radio domain, which consists of a Tx, a channel, and an Rx. At the Tx, a sequence of pseudo-random binary data in the OOK format is applied to the throttle module, which is used to prevent CPU congestion following real-time simulation. Throttles outputs are applied to (i) virtual sink

modules and (ii) MIMO-Tx modules which output is applied to virtual sink modules. In addition, the MIMO-Tx is provided with the outputs of the virtual sources, which represent feedback data on atmospheric loss L_{Atm} (input) in dB and σ_I^2 (input) of the channel. Since GNU Radio provides a graphical user interface (GUI) to generate and configure signal processing flow graphs, sample time waveforms were generated at the outputs of the MIMO-Tx (links A and B) and the optical Rx as shown in Fig 3.3.3(a-f). Figure 3.2.3(a-c) depict the received signal under a clear channel, where only a single Tx (TxA1 and TxB1) is active at any time given. Additional Txs are activated to ensure link availability based on the channel condition, provided $L_{Atm} \geq L_{Atm} (Thres)$ of 0.3 and $\sigma_I^2 \geq \sigma_I^2(Thres)$ of 0.02, thus meeting the FEC BER limits of 3.8×10^{-3} . Fig. 3.2.3 (d-e) depict the simulated time waveforms in this instance.

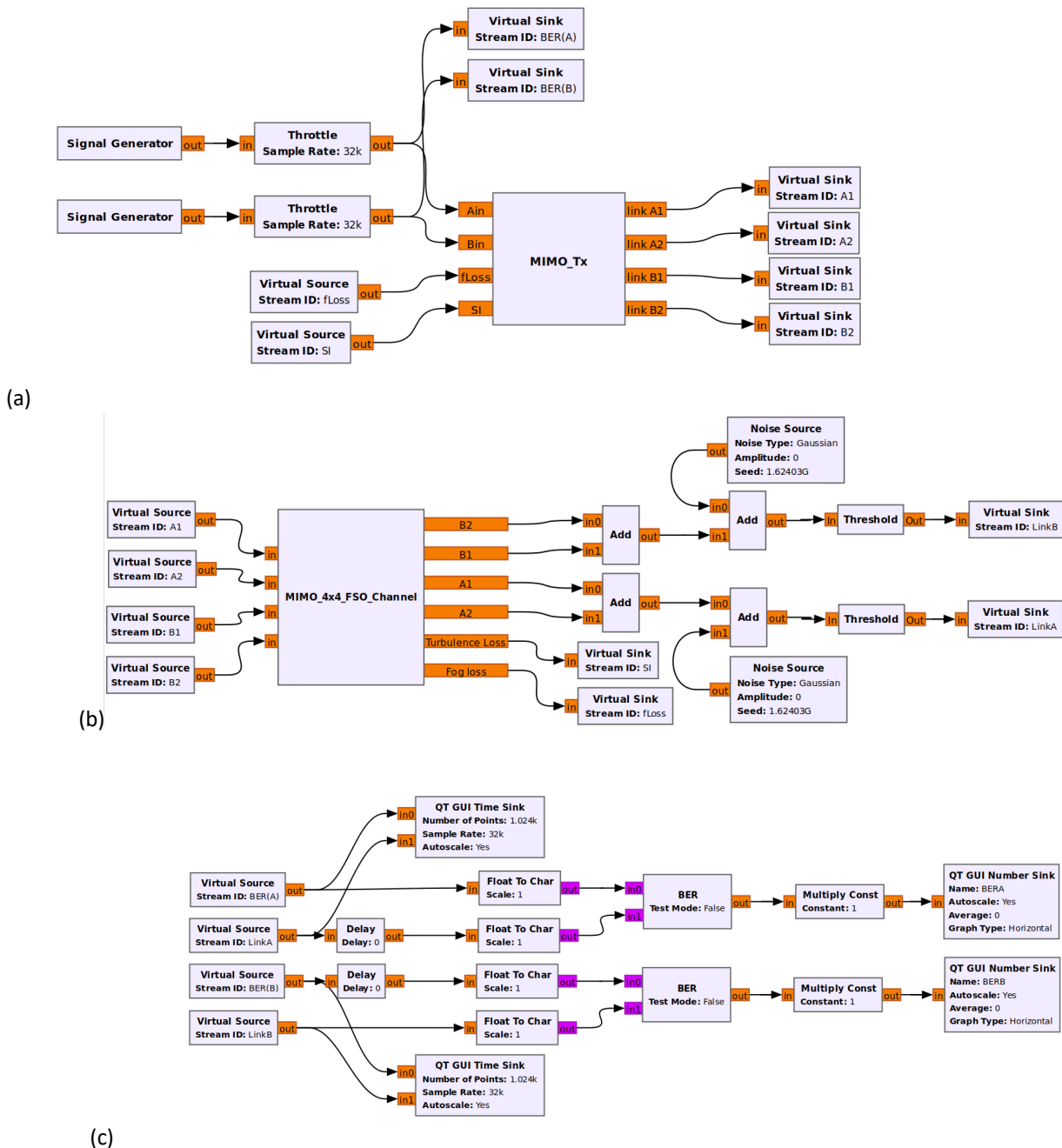


Figure 3.2.2. System implementation for (a) Tx with fog and turbulence, (b) channel with the additive white gaussian noise, and (c) the Rx with real-time BER estimation in GNURadio.

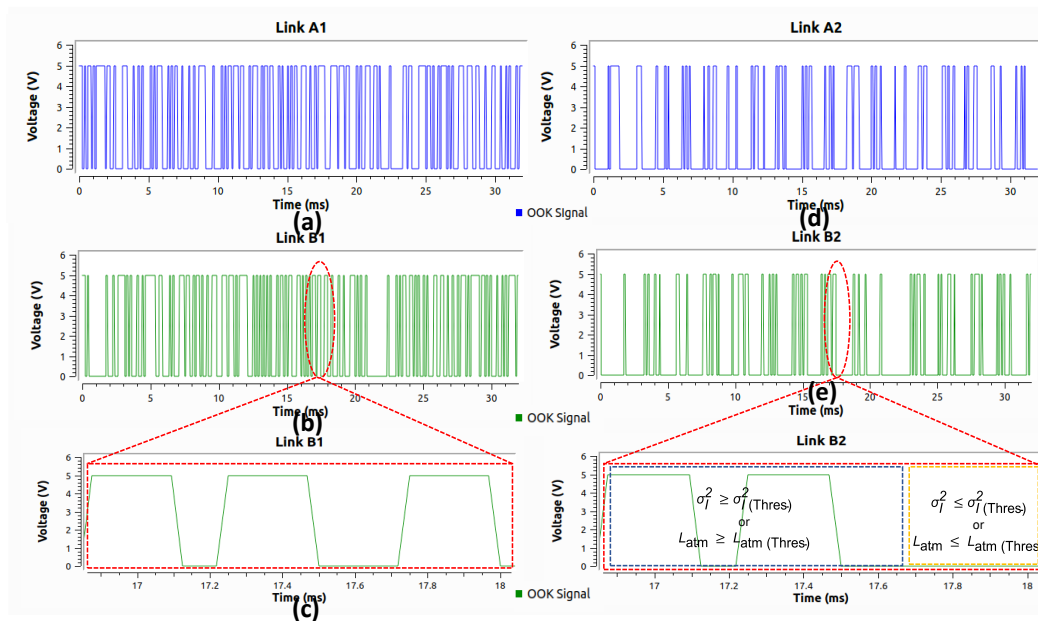


Figure 3.2.3. OOK waveforms at the: (a) Tx-Link A, (b) Tx-Link B, (c) optical Rx for a clear channel, and (d) Tx-Link A, (e) Tx-Link B, and (f) optical Rx for an un-clear channel.

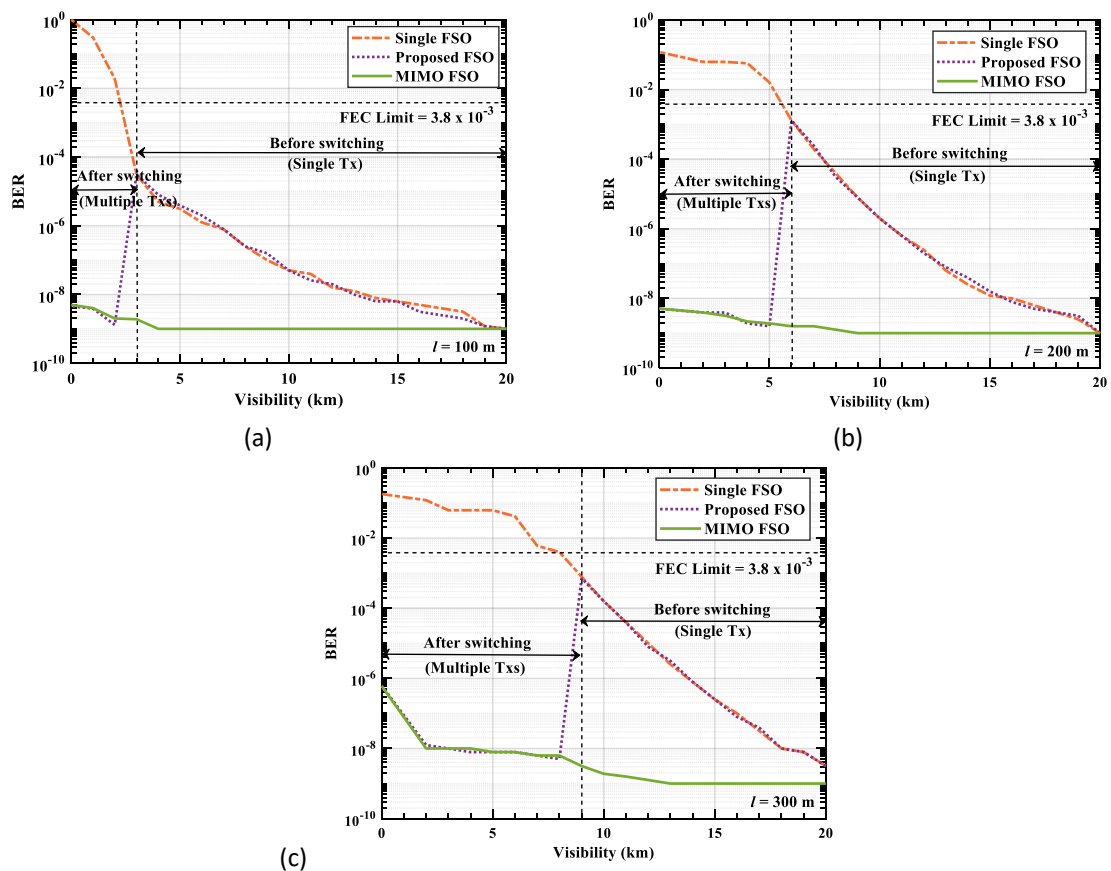


Fig. 3.2.4. BER vs. the visibility for single, MIMO and proposed FSO with adaptive switching links for: (a) 100, (b) 200, and (c) 300 m with fog.

The designed and built OOT not only satisfies the objective to monitor the system performance in real-time, also satisfies the purpose of reconfiguring without the need to change the hardware platform. Moreover, it also offers an easy experimental implementation on the fly due to direct communication with the SDR platform. For a clear channel with V of 20 km, the required P_{Tx} is considered to be 10 dBm with 0 dB channel loss and the additional losses including L_{Geo} are assumed to be low. The system performance in terms of BER for the link range of 100, 200, and 300 m links under the fog conditions are depicted in Fig. 3.2.4. For a 100 m link, MIMO outperforms the single FSO link for $V < 18$ km and especially at lower values of V as expected. For the FSO link with the proposed adaptive switching algorithm, the BER pattern follows the single FSO link, up to a distance of 3 km, after which the BER drops to the MIMO FSO link level with a BER of 10^{-9} which is due to turning on the additional Tx's as explained before. The same pattern is observed for 200 and 300 m links as depicted in Figure 3.2.4 (b) and (c) except when the switching takes place at V of 6 and 9 km where the BER values are at 1.3×10^{-3} and 7.4×10^{-4} , respectively. Also observed are (i) the BER plot for the MIMO FSO link, which is almost constant (i.e., 10^{-9}) at $V > 5$ and 10 km in Figs. 3.2.4(b) and (c). Additionally, compared to D_{Rx} , the beam spot sizes of 17.5 and 34.9 mm in 100 and 200 m, respectively, are smaller. Therefore, L_{Geo} is neglected. Due to the beam spot size of 52.4 mm, an extra 1.2 dB of L_{Geo} is introduced in the 300 m link.

For all three systems, the estimated BER exceeds the FEC limit for $\sigma_I^2 < 0.02$, hence, $\sigma_{I(Thres)}^2$ was set at ≤ 0.02 . The systems were then simulated under weak to moderate turbulence (i.e., $10^{-11} < C_n^2 < 10^{-17} \text{ m}^{-2/3}$) to determine the BER performance for all three systems and link spans of 100, 200, and 300 m as depicted in Figures 3.2.5. In these plots, the same pattern is observed as in Figure 3.2.4 where the BER of the 100 m link adaptive switching the FSO link followed the single FSO link plot for C_n^2 of $10^{-13} \text{ m}^{-2/3}$, beyond which the BER significantly improves, reaching the level of MIMO FSO link at C_n^2 of $10^{-12} \text{ m}^{-2/3}$, from 10^{-4} to 2.5×10^{-8} , see Fig. 3.2.5 (a). This improvement in BER performance is due to the addition of Tx-A2 and Tx-B2. In Fig. 3.2.5 (b), the BER plot for the proposed link changes direction at $C_n^2 < 10^{-14} \text{ m}^{-2/3}$, decreasing to 10^{-8} at $C_n^2 < 10^{-13} \text{ m}^{-2/3}$, and then increasing with C_n^2 . In Figure 3.2.5 (c), the BER transitions from $10^{-3} \text{ m}^{-2/3}$, to 2×10^{-9} at C_n^2 of 10^{-14} to $10^{-13} \text{ m}^{-2/3}$, for the proposed system. Note that, (i) the BER floor level for both MIMO FSO and proposed FSO links is $\sim 10^{-9}$ for $C_n^2 > 10^{-13} \text{ m}^{-2/3}$, and (ii) the 200 and 300 m long MIMO FSO link performance degrades more under turbulence effects (i.e., $C_n^2 > 10^{-13} \text{ m}^{-2/3}$).

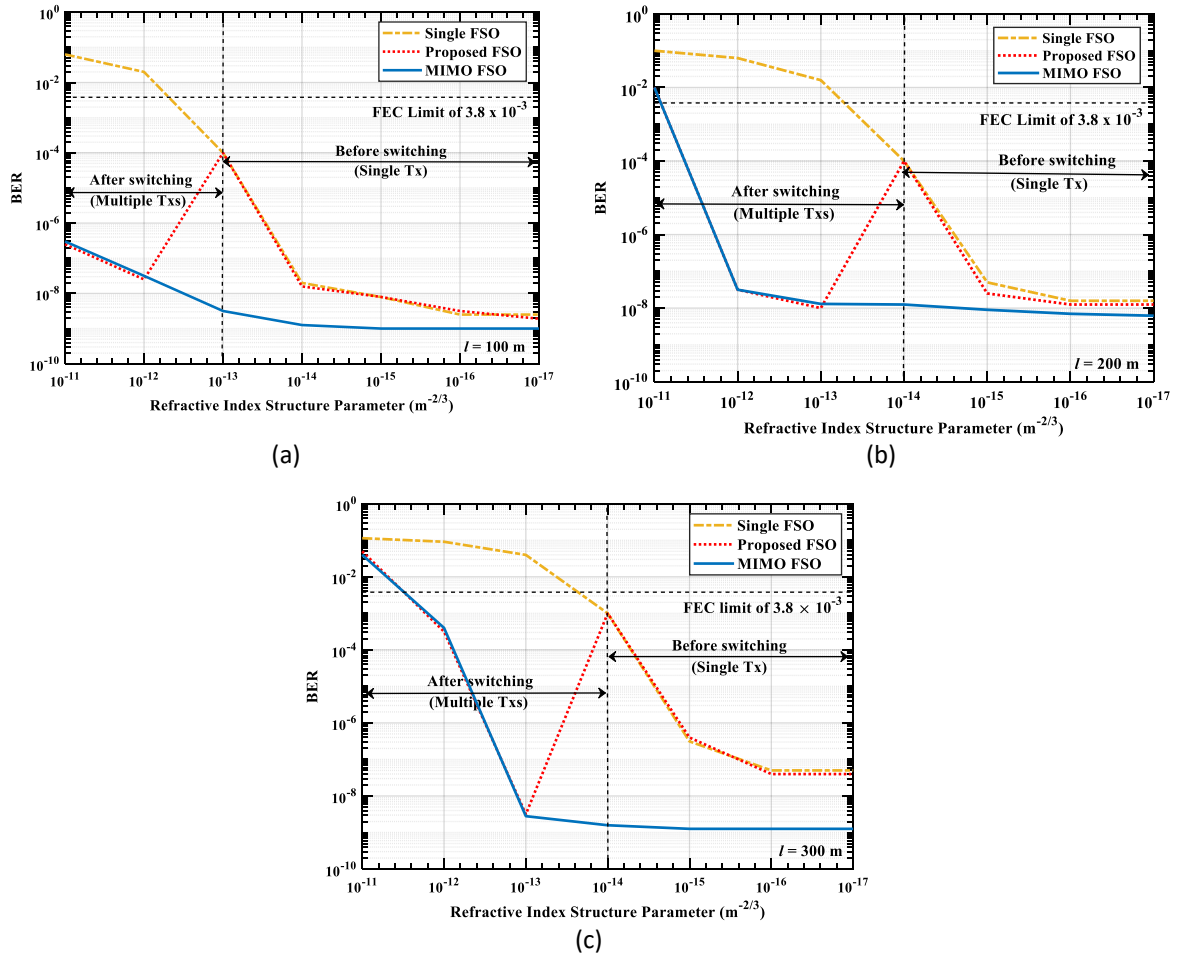


Figure 3.2.5. BER vs. C_n^2 for single, MIMO and proposed FSO with adaptive switching links for: (a) 100, (b) 200, and (c) 300 m with turbulence.

3.3. Transceivers for MMW radio signal over FSO

3.3.1. Photonic mmW signal generation and transmission over fiber/FSO hybrid fronthauls.

Optical transceivers including local and remote photonic mmW signal generation were considered are evaluated in this section by obtaining the analytical expressions of the detected signals after photodetection. Figure 3.3.1 shows a DML located at the BBU, emitting an optical carrier centered at the angular optical frequency ω_0 , which is modulated by data in both schemes [60].

On the one hand, in the local configuration depicted in Figure 3.3.1(a), the optical signal emitted by the DML is launched into the standard single mode fiber (SSMF) and then, it is up-converted by the single tone signal with an angular modulation frequency given by $\omega_{RF} = 2\pi f_{RF}$ in the MZM, which is biased at null point for carrier suppressed modulation. However, in the remote configuration scheme depicted in Figure 3.3.1 **Error! Reference source not found.**(b), the DML output signal is launched into the CS-MZM to be modulated by an electrical single tone signal at $f_{RF}=20$ GHz and then, the resulting signal is transmitted through a SSMF link. The analytical expressions obtained for the photocurrent after photodetection are presented in *Table 3.3.1* at baseband and mmW band for optical back-to-back (OB2B), local and remote configurations [61].

Figure 3.3.2 shows the theoretical system response and the corresponding electrical power measurement at baseband and mmW band for the recovered signal after photodetection [60]. Experimental measurements have been obtained employing a DML (Optical Zonu, OZ516) with a 3 dB bandwidth of 7.75 GHz and the system frequency response has been measured using a signal generator (Rohde Schwarz, SMW200A) and a signal analyzer (SA) (Rohde Schwarz, FSW43).

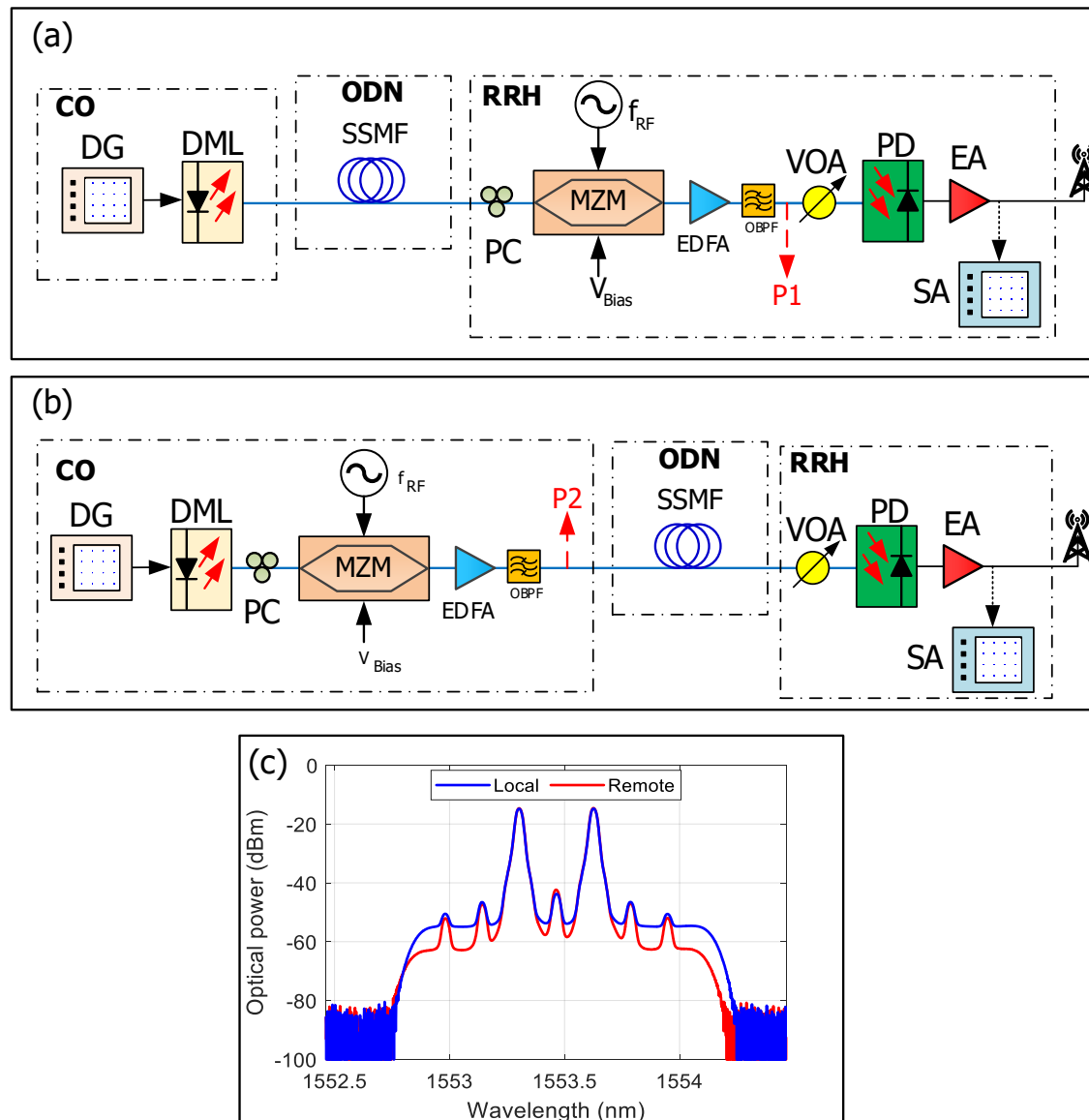


Figure 3.3.1. Experimental setups for: (a) local microwave photonics (MWP) signal generation, (b) remote MWP signal generation and (c) optical spectrum of optically carrier suppressed modulated signal over 25 km SSMF at P1 in setup (a) –blue– and P2 in setup (b) –red–. CO: central office, DG: digital generator, DML: directly modulated laser, PC: polarization controller, MZM: Mach Zehnder modulator, EDFA: erbium doped amplifier, OBPF: optical band pass filter, ODN: optical distribution network, SSMF: standard single mode fiber, RRH: radio remote head, PD: photodetector, EA: electrical amplifier, SA: signal analyzer.

TABLE 3.3.1. ANALYTICAL TERMS OF THE PHOTOCURRENT $i(t)$ AT BASEBAND AND MMW BAND IN OB2B, LOCAL AND REMOTE CONFIGURATIONS.

CONFIG.	$i(t)$	
OB2B	$\Re P_o m_{AM} \cdot [\cos^2 \varphi_{DC} + 2m_{RF}^2 \sin^2 \varphi_{DC}]$	(1)
ω	LOCAL $\Re P_o m_{AM} [\cos^2 \varphi_{DC} + 2m_{RF}^2 \sin^2 \varphi_{DC}] \cdot \left[\sqrt{1 + \alpha^2} \cos \left(\frac{1}{2} \beta_2 L \omega^2 + \text{atan } \alpha \right) + j \alpha \frac{\kappa P_o}{\Omega} \sin \left(\frac{1}{2} \beta_2 L \omega^2 \right) \right]$	(2)
	REMOTE $\Re P_o \left[\sqrt{1 + \alpha^2} \cos \left(\frac{1}{2} \beta_2 L \omega^2 + \text{atan } \alpha \right) + j \alpha \frac{\kappa P_o}{\Omega} \sin \left(\frac{1}{2} \beta_2 L \omega^2 \right) \right] \cdot [m_{AM} \cos^2 \varphi_{DC} + 2m_{AM} m_{RF}^2 \sin^2 \varphi_{DC} \cos(\beta_2 L \omega_{RF} \Omega)]$	(3)
OB2B	$\Re P_o m_{AM} m_{RF}^2 \sin^2 \varphi_{DC}$	(4)
$2\omega_{RF} \pm \omega$	LOCAL $\Re P_o m_{AM} m_{RF}^2 \sin^2 \varphi_{DC} \cdot \left[\sqrt{1 + \alpha^2} \cos \left(\frac{1}{2} \beta_2 L \omega^2 + \text{atan } \alpha \right) + j \alpha \frac{\kappa P_o}{\Omega} \sin \left(\frac{1}{2} \beta_2 L \omega^2 \right) \right]$	(5)
	REMOTE $\Re P_o m_{AM} m_{RF}^2 \sin^2 \varphi_{DC} \cdot \left[\sqrt{1 + \alpha^2} \cos \left(\frac{1}{2} \beta_2 L (\omega^2 \pm 2\omega_{RF} \omega) + \text{atan } \alpha \right) + j \alpha \frac{\kappa P_o}{\Omega} \cdot \sin \left(\frac{1}{2} \beta_2 L (\omega^2 \pm 2\omega_{RF} \omega) \right) \right]$	(6)

Experimental optical OB2B signals both at baseband and mmW band are shown in Figure 3.3.2(a) and (b), respectively. Both transfer functions are proportional to the laser frequency response, which corresponds to the planar theoretical frequency response at baseband and mmW band, respectively. Figure 3.3.2 (c) and (d) show the response for local configuration and, in this case, both bands show similar frequency dependence. Theoretical calculations lead to a dispersion induced power fading for a laser directly modulated signal at frequencies given by:

$$\omega_n \approx \sqrt{\left| \frac{(2n+1)\pi + 2 \text{atan } \alpha}{\beta_2 L} \right|} \quad (n = 0, 1, \dots) \quad (7)$$

A 25 km fiber link leads to the first null ($n = 0$) at the frequency of 15.5 GHz, which is, however out of the laser operating bandwidth. Basically, the term related to phase contribution by means of κ is not significant in this RF frequency range. Experimental measurements at baseband and mmW band are limited by the laser modulation bandwidth and, therefore, show strong similarities to OB2B characterization.

However, the remote configuration leads to a system response, which is significantly different for both bands. According to eq. (3), the first factor leads to the same nulls obtained in (7), which are out of the measuring frequency range. In this case, there are also nulls at frequencies causing the cancellation of the second factor in (3), which are given by:

$$\omega_n = \frac{(2n+1)\pi}{2} \frac{1}{|\beta_2| L \omega_{RF}} \quad (n = 0, 1, \dots) \quad (8)$$

The first null ($n = 0$) is obtained at 3.7 GHz for 25 km SSMF link, as shown in Figure 3.3.2(e) both in the theoretical and experimental curves.

On the contrary, the remote configuration at mmW band (see eq. (6)) only includes the term with nulls at frequencies given by (7), and therefore, no nulls are found within the laser bandwidth (see Figure 3.3.2(f)). However, it is striking that the estimation of (6) at low frequencies, also confirmed by the experimental measurement, leads to a higher amplitude signal under the remote scheme compared to the local configuration as a result of the combined effect of dispersion and laser chirp, as has been previously observed [62]. A signal gain of 15 dB with respect to local or OB2B configurations is

measured for frequency values up to 8 GHz transmitted over 40 GHz. Note that this behavior is not shown in baseband, as explained above.

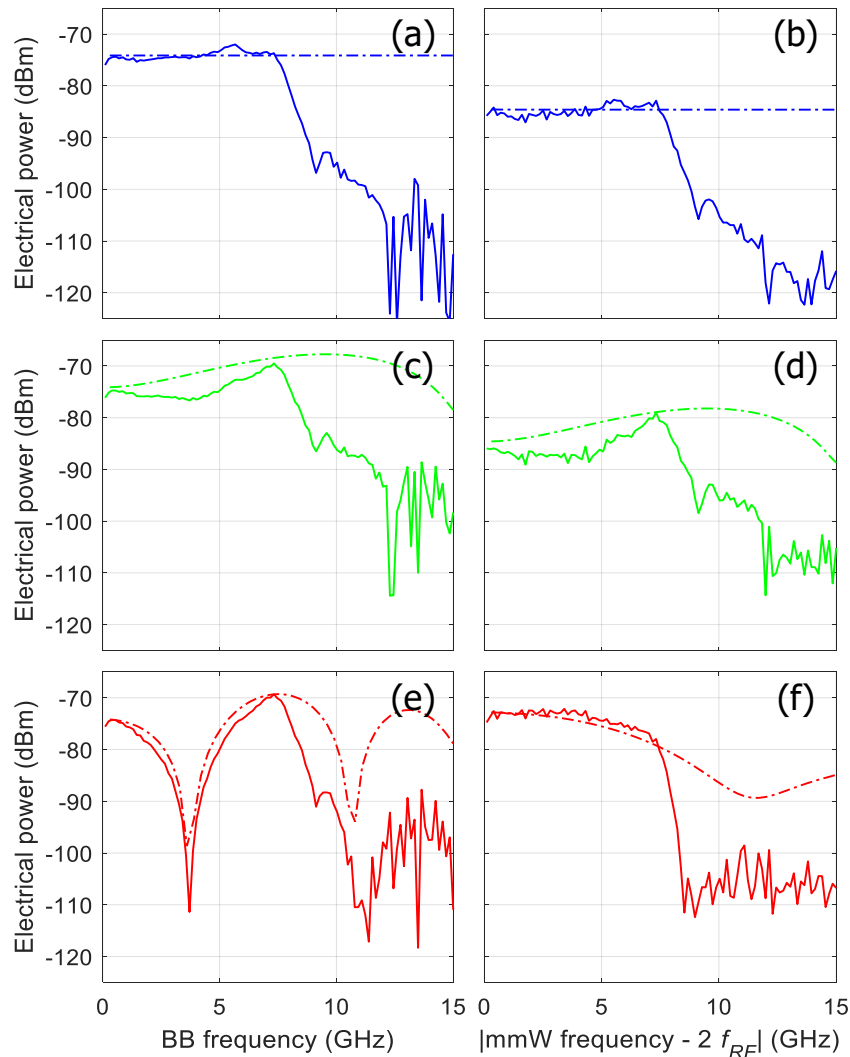


Figure 3.3.2. Comparison of theoretical (dashed lines) and experimental (solid lines) electrical output power at baseband (left side) and mmW (right side) band: (a)-(b) OB2B, (c)-(d) local and (e)-(f) remote configurations, respectively. Both local and remote configurations are obtained over 25 km SSMF link.

The recovered electrical spectra after photodetection for OB2B, local and remote setups are depicted in Figure 3.3.3 [60]. The mmW signal with -27.6 dBm electrical power is generated at 40 GHz, as shown by the electrical spectrum measured under OB2B setup in Figure 3.3.3 (a). The extinction ratio with respect to the original carrier at 20 GHz is higher than 36 dB, the insets show the detail of the data band at baseband (-75 dBm) and also at mmW band (-82 dBm).

Figures 3.3.3 (b) and (c) correspond to measurements under local configuration for 10 and 25 km SSMF, respectively, and lead to similar electrical power levels than OB2B both for baseband and mmW band, according to Fig 3.3.3(c) and (d) (also in good agreement with eqs. (2) and (5)).

On the other hand, Figures 3.3.3 (d) and (e) show the measured electrical spectra for 10 and 25 km SSMF remote setup and no significant differences are found in data baseband with regards to OB2B.

However, an electrical power increase of 9 and 16 dB is observed in data bands carried by mmW signal after transmission over 10 and 25 km fiber link, respectively. This fact confirms the results presented above, where the electrical amplitude at the mmW band under remote configuration was found to be 15 dB larger with respect to OB2B (eq. (6) and Figure 3.3.2(f)) due to the system response. However, the remote configuration leads to high intermodulation (IMD) products at 40 GHz band in 25 km fiber link (see inset in Figure 3.3.3 (e)). Note that local configuration over the same link, shown in Figure 3.3.3 (d), does not exhibit IMD signals, which can lead to dramatic penalties under certain signal conditions in remote generation setup, i.e. large bandwidth or multiband signals. Also, small residual bands appear around 20 GHz due to the lack of perfect carrier suppression in the MZM, which are more visible after the 25 km SSMF link.

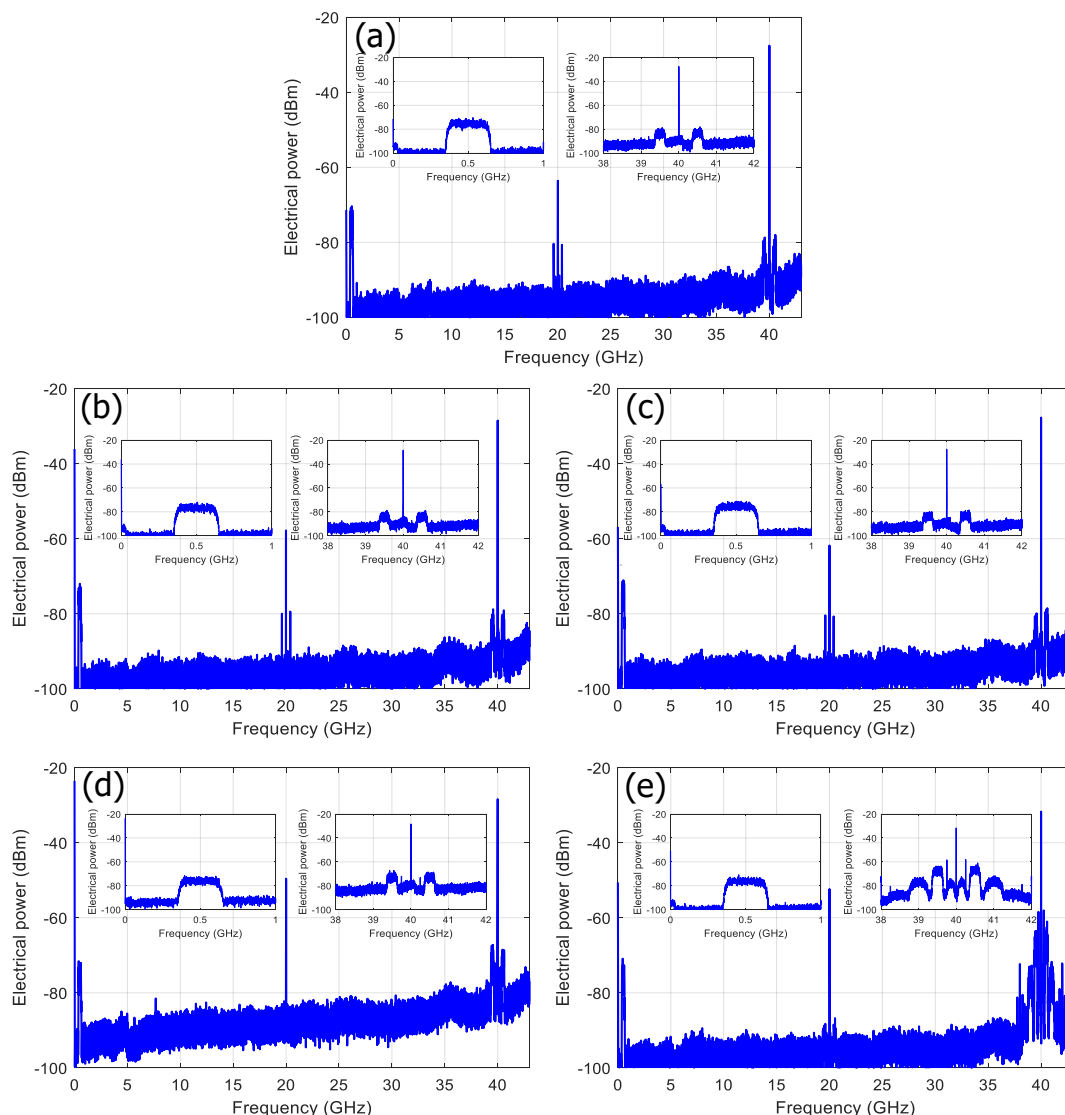


Figure 3.3.3. Measured electrical spectra after photodetection with different configurations: (a) OB2B, (b) Local signal generation with 10 km fiber link, (c) Local signal generation with 25 km fiber link, (d) Remote signal generation with 10 km fiber link, (e) Remote signal generation with 25 km fiber link; insets show the detail of the data band at baseband and at mmW band.

The experimental work is completed by evaluating the system performance for different frequencies in order to confirm the theoretical and experimental frequency system response presented in Figure 3.3.2. Figure 3.3.4 shows EVM measurements and electrical received power as a function of the central frequency of the 250 MHz bandwidth QPSK signal both at baseband and at mmW band for OB2B, local and remote setups over 25 km fiber link [60].

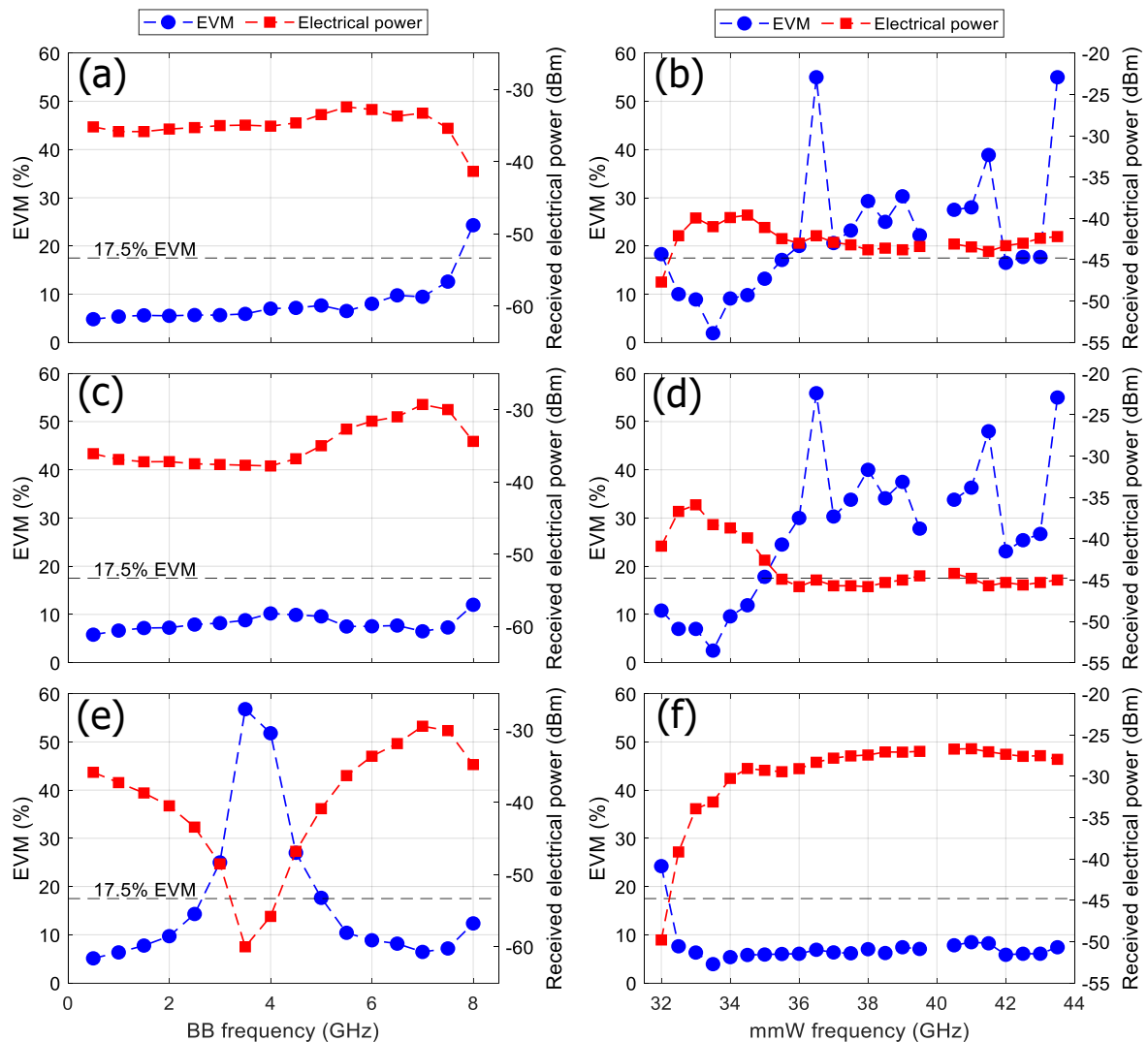


Fig. 3.3.4. EVM and received electrical power for different setups vs frequency over 25 km fiber link: (a)-(b) OB2B, (c)-(d) Local setup and (e)-(f) Remote setup, at baseband and millimeter wave band, respectively.

Figure 3.3.4(a) shows a clear correlation between EVM and electrical power for OB2B, since they result from the DML frequency response (see Figure 3.3.2 (a)). Electrical power decreases (i.e. EVM increases) due to the 7.75 GHz bandwidth limitation on the DML, so measurements are shown up to 8 GHz. Accordingly, measurements in the mmW band have been done from 32 GHz (8 GHz below the 40 GHz band) up to 43.5 GHz due to the SA bandwidth limitation. Again, the electrical power follows the predicted behavior of the theoretical frequency response (see Figure 3.3.2(b)) with corresponding EVM values where several EVM fluctuations are observed above the threshold.

Figure 3.3.4(c) shows the electrical power and EVM measurement against frequency in baseband for local setup following the measured frequency response in Figure 3.3.2(c), which is similar to the one measured in OB2B setup. However, Figure 3.3.4(d) shows some reduction (i.e. 2.5 dB at 35.5 GHz) of the electrical power with respect to the OB2B although a maximum is obtained at 7 GHz offset respect to 40 GHz, due to DML frequency response and also according to Figure 3.3.2(d). Again, higher EVM values with some fluctuations due to signal processing are obtained above the threshold.

Finally, the performance of the remote generation setup is also characterized in frequency. Figure 3.3.4(e) shows the electrical power decrease (i.e. EVM increase) at 3.7 GHz for remote setup, in good agreement with the notch predicted by eq. (8) in baseband frequency response. However, Figure 3.3.4(f) shows a 13 dB increase of electrical power (i.e. reduced EVM) with respect to OB2B along the measurement frequency range up to 35.5 GHz (4.5 GHz below 40 GHz) in accordance to Figure 3.3.2(f).

3.3.2. Phased beamforming in optical domain

The transmission of high frequencies, i.e., millimeter wave (mmW), has significant path and penetration losses. One practical solution to compensate for the higher losses is to deploy a large-scale phased antenna array (PAA) to achieve high PAA gain in a high frequency system due to the smaller wavelength [63]. An example of this is a base station operating at 30 GHz with a 200-meter-transmit range and needing 60 dBm effective isotropic radiated power (EIRP) for a reasonable signal-to-noise ratio (SNR) at the receiver. This is almost impossible to achieve using a single element transmitter. However, if, for example, a 100-element PAA transmitter is used, only 20 dBm output power is required from each element of the phased array, which is reasonable with today's low-cost fully integrated solutions [64]. Along with the use of microwave photonics in RF networks, the optical system enables beamforming by employing variable true-time delay (TTD) modules to introduce a phase difference in particular PAA elements [65]. One of the approaches for optical TTD for an mmW frequency band is the usage of the chromatic dispersion phenomenon with a multi-wavelength optical signal allowing phase delays to be optically set up for different wavelengths. We have realized, for the first time, an experimental validation of data transmission in the 24-28 GHz band using optical beam steering via chromatic dispersion in a hybrid RF/optical system. For this purpose, we have proposed a microwave photonic link (MPL) in a given band with an in-house built application-tailored three-element PAA based on planar dipoles to provide enough beam steering scalability. We have demonstrated PAA beam steering performance and confirmed the usability of our approach within a microwave photonic network by evaluating data transmission quality over a 1.5-m-long wireless distance.

The complete experimental demonstration of beamforming carried out in MPL has been realized according to the scheme in Fig. 3.3.5 [66]. A tunable 3-port laser source (CoBrite DX4) is used to adaptively control the phase difference between particular link outputs feeding the PAA due to the effect of chromatic dispersion in the optical fiber. Each of the three ports of the laser source (providing signals at 1534.695, 1550.031 and 1571.178 nm, all with optical power 16 dBm) is connected via polarization controllers (PCs) to the CWDM to combine the signals into a single SMF. After multiplexing, the signals pass through another PC adjusting the polarization state to the MZM (Optilab IML-1550-50-PM), which serves as an electrical-to-optical convertor. The MZM is biased in a quadrature operation point corresponding to a bias voltage of 0.8 V. Note that the MZM allows the modulation of

all three optical carriers by an identical RF signal. A 10-km-long SMF is employed to emulate the distance coverage of the radio signal in a real network. The SMF allows chromatic dispersion-induced time delay between particular optical carriers by introducing a phase delay for the RF signals. This particular SMF length also avoids the chromatic dispersion induced RF power fading. At the output of the SMF, the CWDM divides particular carriers, according to their wavelength, into three optical branches which are terminated by PDs (Optilab PD40). The PDs transform the optical signals back to the RF domain. To reach sufficient RF power for radiating the signal from the PAA to free space, three identical RF electronic amplifiers (EAs, Analog devices HMC1131) are deployed with an average gain of 21 dB over the 24 – 35 GHz band. Finally, the PAA is connected to the EAs via 10-cm-long coaxial cables with mini-SMP connectors. Note, to reduce unwanted reflections in our experiment, the PAA, with EAs, PDs and the WDM demultiplexer, has been placed on a rotating board and characterized within an anechoic chamber situated at the Czech Technical University in Prague, Faculty of Electrical Engineering. The PAA-transmitted CW signal is received after a 3-m-long wireless propagation in the chamber by a double-ridged horn antenna (RFspin DRH40 with 15 dBi gain at 25 GHz), amplified by low-noise EA (Miteq AMF-4F-260400-40-10p) and delivered to the receiver. To obtain the radiation pattern of the PAA, a vector network analyzer (VNA, Rohde & Schwarz ZVA40) is used, whereas for data transmission, the combination of the signal generators (Rohde & Schwarz SMW200A, SMF100A), RF mixer and spectral analyzer (Rohde & Schwarz FSW) is leveraged. The system operates in a transmitting mode. However, the proposed system could also be used in receiving mode.

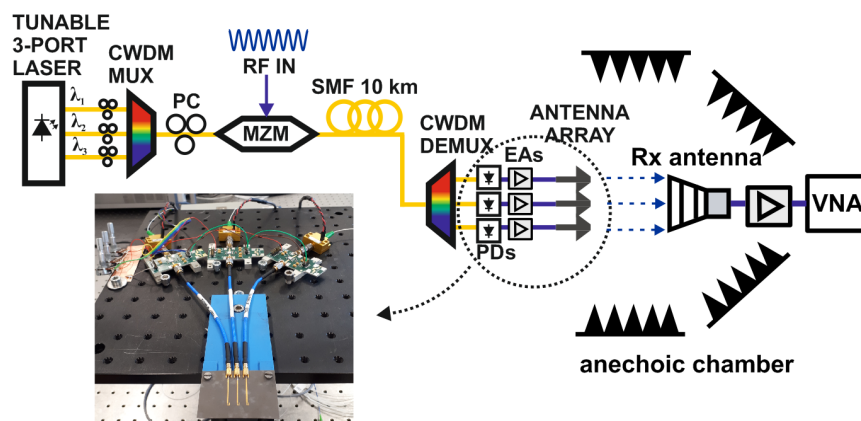
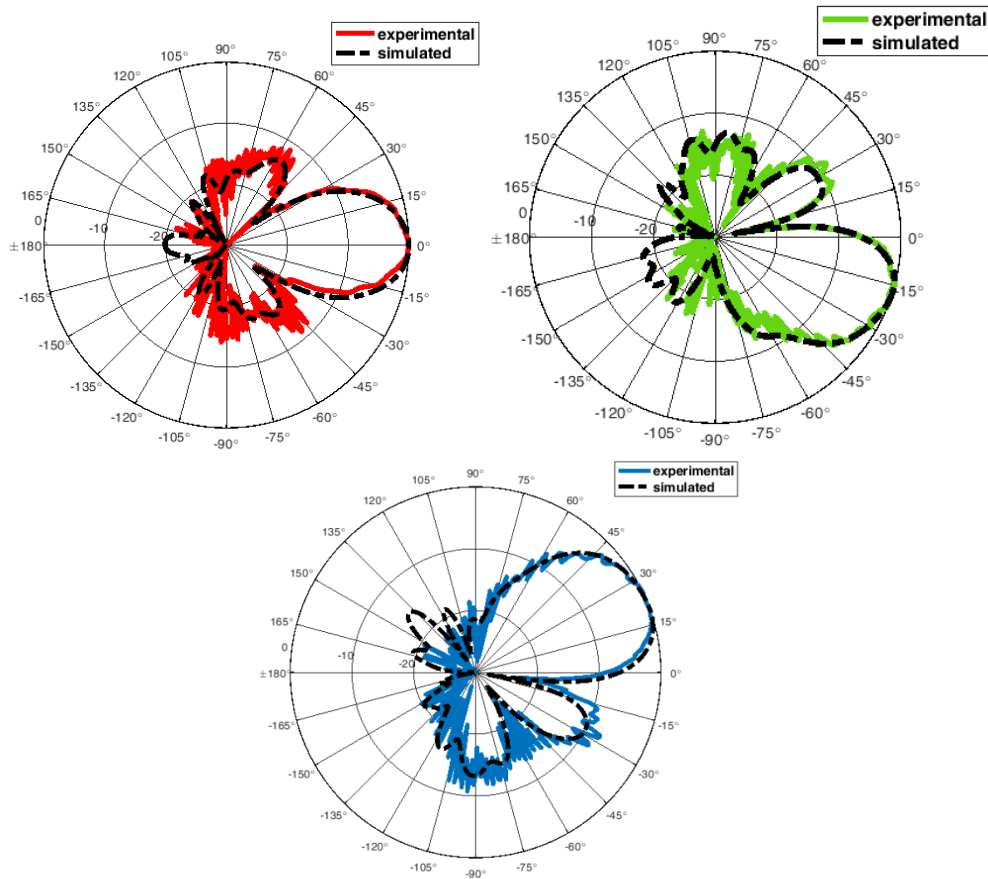


Fig. 3.3.5 Experimental setup of an RoF link for mmW transmission and optical-controlled beamforming.

Selected results for the frequency of 26 GHz with steering angles of 0°, -25° and 25° are shown in Fig. 3.3.6 a), b) and c), respectively [66]. For the sake of comparison, black dashed lines denote simulated results obtained by CST Studio Suite. Meanwhile Fig 3.3.6a) shows the radiation pattern with no phase difference among the PAA elements, Fig 3.3.6 b) and c) depict the radiation pattern of the system with an introduced phase difference of $\pm 80^\circ$ from the middle element to steer the wavefront in the desired angle, i.e., $\pm 25^\circ$. Note that these measurements have been carried out for a single-tone signal without any modulation (i.e., data).



*Fig. 3.3.6 Measured and simulated radiation patterns at 26 GHz for steering angles
a) 0° b) -25° and c) 25°.*

A data signal was added to analyze our hybrid system performance for practical use within the given bandwidth. For these purposes we transmitted the signal from the PAA over a distance of 1.5 m of free-space. For signal generation, a baseband generator (R&S SMW200A) was used with predefined cellular network test models according to the long term evolution (LTE), and test model TM 3.1 using 64-quadrature amplitude modulation (QAM) was adopted. This model is, in general, proposed to test transmitted signal quality and output power dynamics [67]. The baseband was up-converted to the desired frequency by using a mixer and signal generator (R&S SMF100A) serving as a local oscillator with a frequency of 25 GHz. The signal was subsequently amplified by using an EA (Analog devices HMC1131) which led to the MZM RF input, so all three optical carriers carried the same RF signal. At the receiver side, a spectral analyzer (R&S FSW) was used for the demodulation and data evaluation. Note that this measurement was performed outside the anechoic chamber.

In the first series of tests, with regard to the previous experiment, we set the steering angle to 0° and 25° by tuning the laser to the above-mentioned wavelengths and then measuring received power and error vector magnitude (EVM) with the dependence on the PAA azimuth in the range of $\pm 60^\circ$. Test model 3.1 was used with 64-QAM and 20 MHz bandwidth resulting in a data throughput of 75 Mb/s. Fig. 3.3.7 shows the result for a 0° steering angle, while Fig. 3.3.8 depicts results for 25° [66]. EVM performance, in terms of constellation diagrams for 64-QAM, is shown in the azimuths of -25, 0 and 25°.

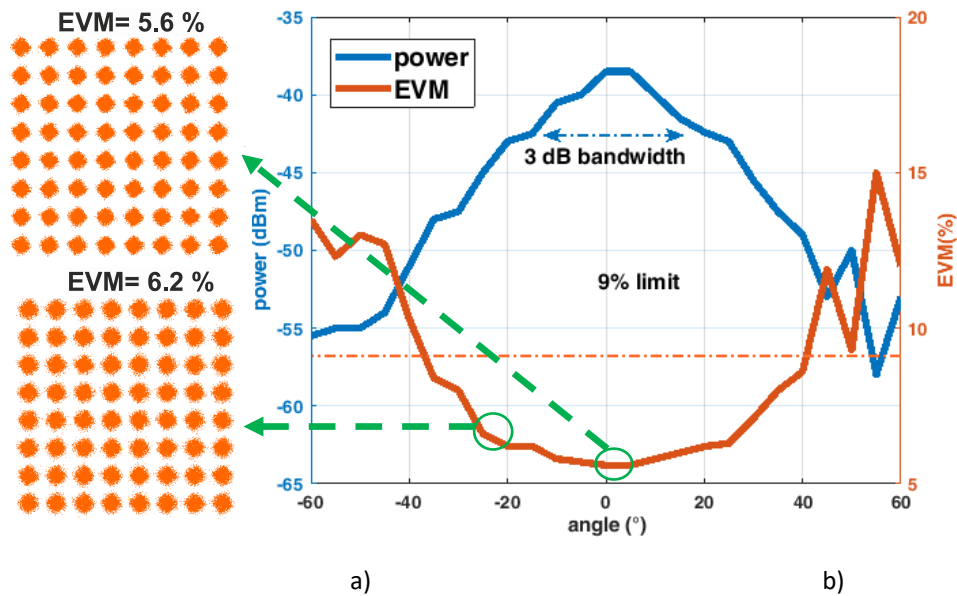


Fig. 3.3.7 EVM and received power vs. PAA azimuth angle at 25 GHz for 64-QAM signal with 20 MHz bandwidth for steering angle 0°. Constellation diagrams are shown at azimuth 0° and -25°.

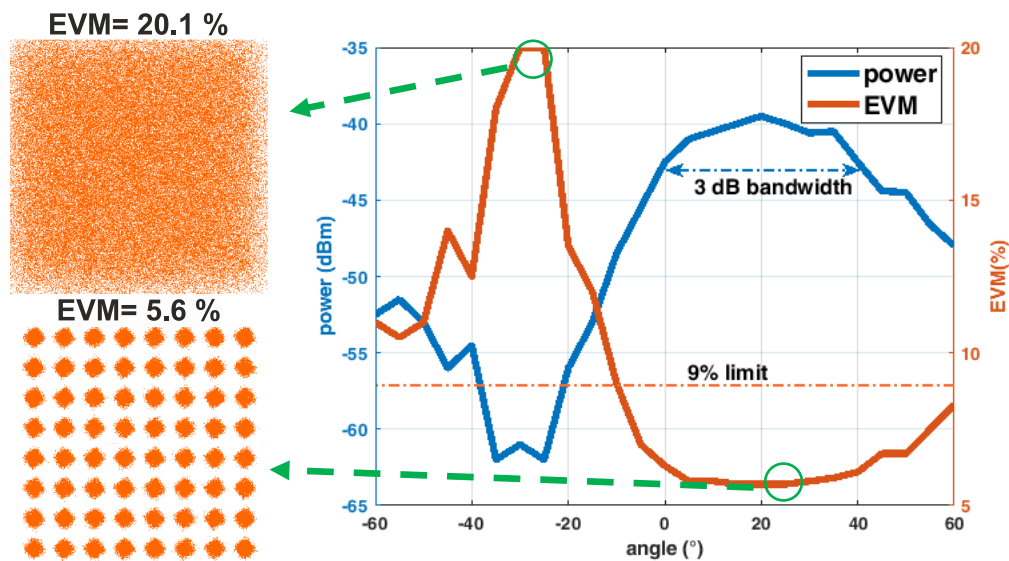


Fig. 3.3.8 EVM and received power vs. PAA azimuth angle at 25 GHz for 64-QAM with 20 MHz bandwidth for steering angle 25°. Constellation diagrams are shown at azimuth -25° and 25°.

3.3.3. Integrated transceiver – tests within relay system

One of the key aspects of the RoF technology is its capability to realize a seamless analog RF signal transmission without the need for signal processing following optical-to-electrical (OE) conversion and prior to transmission via an antenna. This feature enables a high number of electrical-to-optical (EO) and OE conversions, which can be used to provide additional wireless connectivity. Moreover, the RoF technology can be supplemented with a free space optics (FSO) link where the use of fiber cables is not possible or expensive. In this case, a radio over FSO (RoFSO) system can be realized to provide a flexible mobile fronthaul transmission from a central office (CO) to base stations (BSs). On the other

hand, RoF systems can also be utilized for transparently relaying radio signals from outdoor to indoors to avoid penetration losses, especially for radio signals in the high frequency bands. The concept of a cascade of a RoF/RoFSO mobile fronthaul, mmW radio access network (RAN), and indoor RoF relay system for the mmW indoor coverage in a mobile network is illustrated in Fig. 3.3.9 [68].

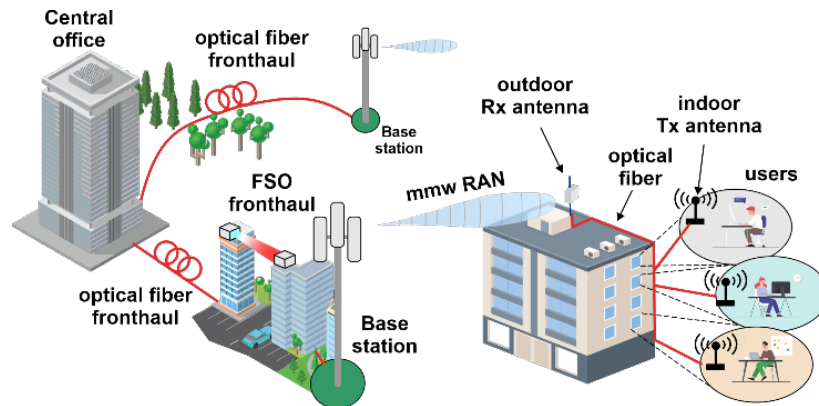


Fig. 3.3.9. The proposed end-to-end mmW signal transmission for indoor networks using RoF and RoFSO systems.

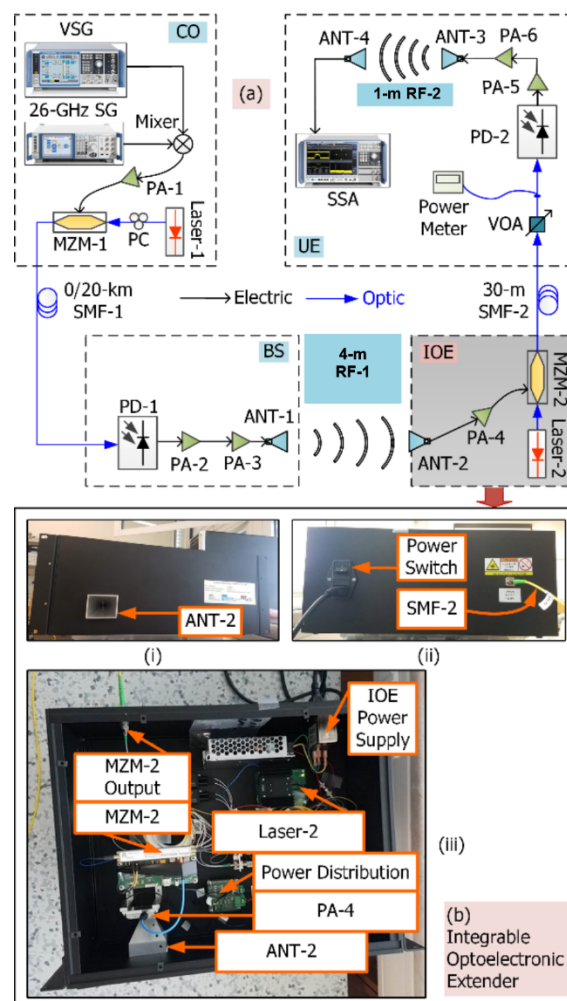


Fig. 3.3.10. (a) Experimental setup for mmW signal transmission over a cascaded RoF mobile fronthaul, mmW RAN, and RoF relay system; (b) compact prototype of the mmW IOE.

We have demonstrated for the first time an end-to-end transmission of a 26 GHz signal from a CO to an indoor end user using RoF/RoFSO systems. For the use of RoF mobile fronthaul, a simple optical double sideband signal transmission was transmitted over a 20-km SMF without using an optical amplification. For the case of RoFSO mobile fronthaul, an optical single sideband (SSB) signal was transmitted and an EDFA was utilized to extend the fiber reach for the fronthaul network. The extension of the proposed setup was realized with the main emphasis on the first optical section because a considerably longer SMF-1 link can be expected compared to SMF-2, which only serves for indoor coverage. To increase the distance of the SMF-1 link, we generated and transmitted an optical SSB signal. Further, we inserted an FSO link to the SMF-1 to emulate the usage of the RoFSO system for mobile fronthaul transmission from the CO to the BS. We updated the first optical section of the scheme from Fig. 3.3.10, as shown in Fig. 3.3.11(a) [68]. The output signal from CO is launched to the optical channel by the dense wavelength division multiplexing (DWDM) multiplexer with a 0.8 nm grid (100 GHz).

Simultaneously, the wavelength of the Laser-1 is tuned to the wavelength of 1548.67 nm, while the center wavelength in the corresponding channel is 1548.51 nm. Thus, the intensity modulated optical carrier, operating in the DSB regime with side bands ± 26 GHz, is turned into the SSB transmission due to the filtering of one sideband out by the DWDM; see corresponding optical spectra in Fig. 3.3.11(b).

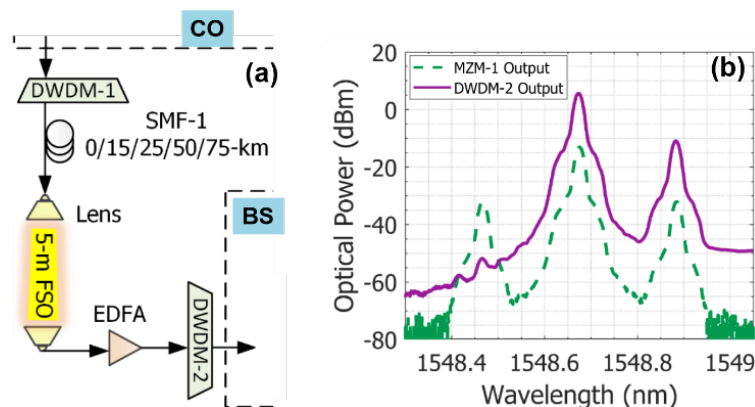


Fig. 3.3.11 (a) The experimental setup using the RoFSO system in the mobile fronthaul; (b) optical spectra before and after the DWDM-1.

The SSB transmission scheme is immune to CD-induced fading, and thus almost any length of the SMF can be used. It should be noted that SMF-2 link, operating in DSB regime at ± 26 GHz, perfectly withstands the CD fading for the considered indoor range, which is expected within 100 m. Furthermore, a 5 m long FSO channel, realized by a pair of doublet collimators (Thorlabs, F810APC-1550), is implemented to provide better flexibility. An EDFA (Keopsys CEFA-C-HG-SM-50-B130-FA-FA) is employed to compensate for additional losses of longer fiber section and 6 dB insertion loss (IL) of the FSO channel. After the EDFA, the signal is demultiplexed in DWDM-2 demultiplexer. It is worth mentioning that a number of DWDM channels can be exploited, which significantly extends the capacity of the first stage of the setup.

The overall system performance for fiber mobile fronthaul is shown in Fig.3.3.12 depicting the EVM and the BER performance as a function of P_{rO} and P_{rRF} , respectively for 4-, 16-, and 64-QAM [68]. The EVM plots show minimum values at $P_{rO} > 5$ dBm, so to keep the EVM values below a particular EVM

limit, P_{rO} is at least 1.5 and 2.5 dB higher for 4- and 16-QAM, and 64-QAM, respectively, compared with the OB2B. The minimum P_{rRF} to meet the FEC BER limit are -63, -59, and -55 dBm for 4-, 16-, and 64-QAM, respectively.

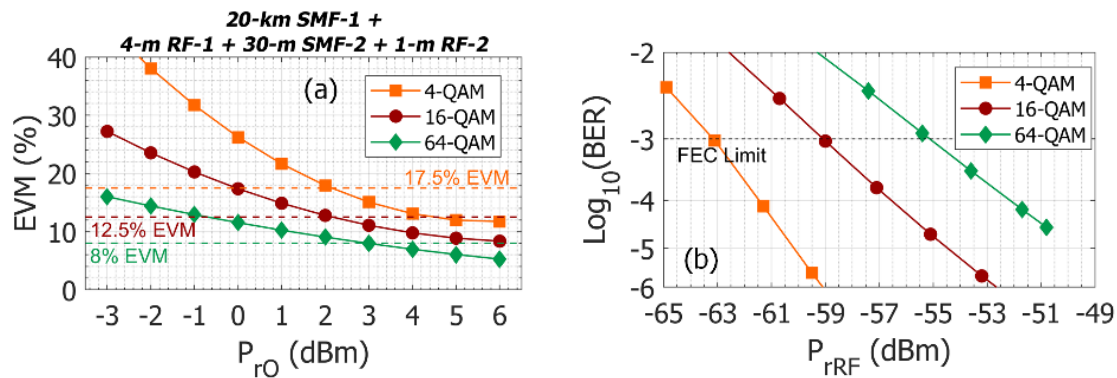


Fig. 3.3.12. The full system performance for 4-, 16-, and 64-QAM: (a) EVM vs. P_{rO} , and (b) $\text{Log}_{10}(\text{BER})$ vs. P_{rRF} .

Fig. 3.3.13 (a) depicts the dependence of the EVM for 64-QAM signal with a 20 MHz bandwidth at 26 GHz on P_{rO} for various SMF lengths and EDFA within the combined fiber fronthaul network with the SSB transmission scheme [68]. It can be seen that up to 75 km is applicable while a wide range, i.e., for P_{rO} between 2 and 6 dBm, maintains the EVM below 8%. In addition, there is only approx. 1 dB penalty between using 15 and 75 km of SMF in the first stage.

Finally, the 5 m long FSO channel in the first optical stage was deployed to make this part of the fronthaul network more flexible. To demonstrate the maximal system performance, a full configuration including 75 km of SMF and 5 m of FSO with the following EDFA in the first optical section was deployed. The RoF relay system was tested with 64-QAM; see results in Fig. 3.3.13(b).

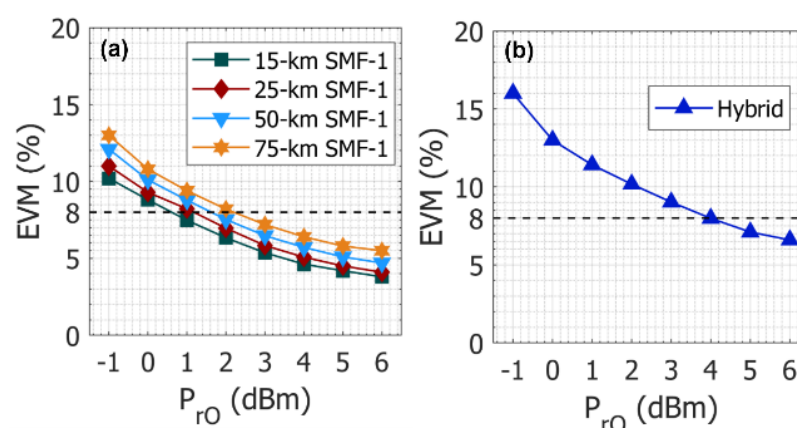


Fig. 3.3.13. The SSB system performance showing EVM for 64-QAM vs. received optical power for: (a) various SMF-1 length, and (b) for the system including 75 km of SMF-1 and FSO.

3.4. Optical Camera based Communication System

The OCC long distance system has been developed. The experiments were carried out with two transmitters built using a 5 mm white LED controlled by an Arduino board and one receiver built using a Raspberry Pi with Camera Module V2. The Tx nodes were placed outdoors from the proximity of the IDeTIC Institute facilities in Las Palmas, Spain, at 90 and 130 m from the receiver placed indoors, as shown in Figure 3.4.1. The key parameters of the experiments are summarized in Table 3.4.1.

Table 3.4.1. Key experiment parameters and values

Metric	Parameter	Value
Tx	Light source	Single 5 mm white LED
	Data rate	7.5 bps
	Microcontroller	Arduino Nano
Channel	Link span (d_1)	90 m
	Link span (d_2)	130 m
Rx	Camera	Raspberry Pi Camera V2
	Frame rate	30 fps

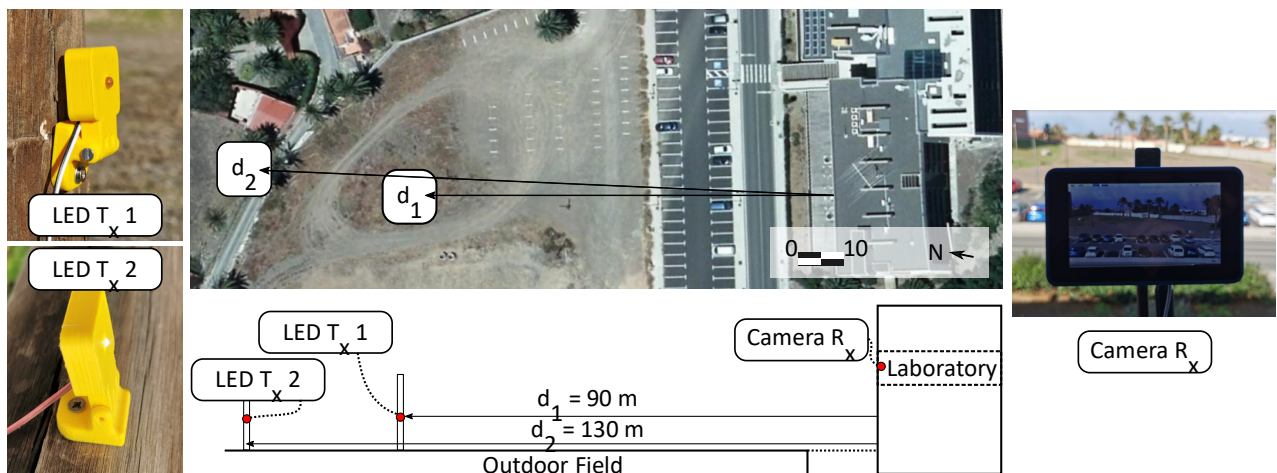


Figure 3.4.1 - Experimental setup

The data frame structure generated at the transmitters comprised a header, guard bits, and one 8-bit payload, with chip time equals 4 image frames captured by the camera, to ensure every bit is captured in the video, considering the framerate of the camera can slightly vary. Then, at the processing stage (done offline), a correlation-based detection allows the system to locate the overhead parts of the frame and then detect the bits, as shown in the diagram in Figure 3.4.2.

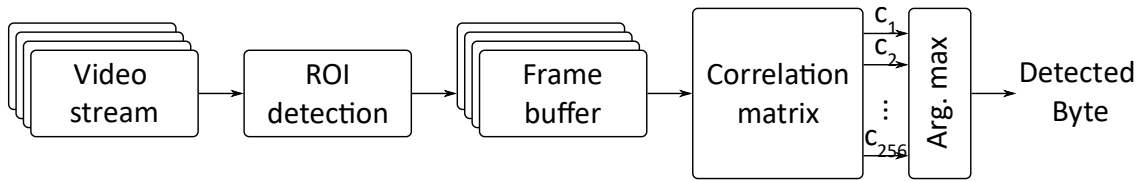


Figure 3.4.2 - Signal detection process

As shown in [24], although the projection of the LEDs over the image sensor was theoretically under the size of one pixel, due to the camera focus configuration and the scattering induced by the channel, more than one pixel contains useful data for each transmitter. This allows the receiver to consider not only the central pixel but surrounding pixels as well. As a result, the weighted-average signal obtained from all the mentioned pixels reached up to 20 dB of signal-to-noise ratio (SNR), as shown in Table 3.4.2.

Table 3.4.2. Key performance results from sub-pixel OCC experimentation

Metric	Position	Channel R	Channel G	Channel B
Experimental SNR	d ₁	19.7 dB	20.0 dB	19.8 dB
	d ₂	13.0 dB	12.9 dB	12.5 dB
Theoretical BER	d ₁	$<10^{-12}$	$<10^{-12}$	$<10^{-12}$
	d ₂	$3.97 \cdot 10^{-6}$	$5.03 \cdot 10^{-6}$	$1.24 \cdot 10^{-5}$
Experimental BER	d ₁	$<3.33 \cdot 10^{-3}$	$<3.33 \cdot 10^{-3}$	$<3.33 \cdot 10^{-3}$
	d ₂	$9.60 \cdot 10^{-3}$	$9.60 \cdot 10^{-3}$	$7.20 \cdot 10^{-3}$

The sub-pixel approach demonstrates the capability of re-utilizing camera equipment for simultaneous image and wireless data acquisition at long-range OCC. Although the achievable data rate per node is considerably low, under ten bps, it can be compensated by increasing the number of nodes parallelly transmitting data to the same camera receiver, potentially reaching thousands of bps. The sub-pixel OCC system is inherently susceptible to being affected by the time-varying wireless channel. Slight deviations of the light caused by turbulence, attenuation caused by the presence of aerosols, and occlusions caused by objects in the scene can easily down the links. Furthermore, discovery and tracking algorithms need to be developed to support node mobility. Considering the capabilities and limitations of the sub-pixel OCC system presented, this approach can be applied to establishing outdoor wireless sensor networks, in which low data rates are required, and nodes can be static in most cases. Furthermore, if mobility is supported, applications in vehicular networks could be addressed.

The feasibility of deploying OCC in atmospheric conditions was first presented in [9], where meteorological phenomena were emulated in a laboratory chamber. This work experimentally evaluated the effects of heat-induced turbulence and the presence of aerosols over a 5 m-long rolling shutter (RS) OCC link. An important contribution of this work was the use of the analog gain parameter of the camera to overcome the effects of dense fog. Furthermore, it was found that the large transmitter projection over the image sensor required for RS OCC makes the effect of turbulence negligible. An algorithm for controlling the analog gain of the camera was then developed in [70]. Later, the effects of a real sandstorm were experimentally assessed in [71], where an RS OCC approach was used to deploy a 200 m-long outdoor link. In this work, it was found that the scattering caused by the

aerosol particles in the air act as a diffuser that enlarges the projection of the transmitter over the camera image sensor, resulting in a higher data rate compared to clear air.

As mentioned before, the RS OCC requires large areas of projection of the transmitter over the image sensor, which can be obtained using extensive transmitters or long camera lenses. To reduce the need for large-scale optical front ends, the subpixel OCC link was proposed in [25], in which small form factor transmitters and receivers could communicate at distances of about 100 m.

4. Conclusions

With the aim of presenting novel achievements obtained within NEWFOCUS Action on transceiver designs as advanced optical PHY solutions for wireless communications, this deliverable mainly reports on MIMO free space optics links, visible light communication OCC systems and millimeter wave signals transmission over fiber and FSO links as relevant technologies in medium-range communications distance.

This document provides a short review of proposed solutions in the previous literature with a focus on the recent achievements for highly reliable FSO and VLC –based transceivers for the first- and last-mile access and backhaul/fronthaul wireless networks.

More concretely, with regards to FSO transceivers, recent demonstrations show that the uni-polar quantum devices, including directly modulated QCLs, external Stark-effect modulators, and QCDs, have progressed fast to a maturity level for system transmissions supporting over 10 Gb/s.

Moreover, a real-time SDR/GNU Radio implementation of a MIMO FSO link has been demonstrated with adaptive switching under different atmospheric conditions, concluding that the proposed switching mechanism mitigated the fog and turbulence induced attenuation for a range of transmission link spans. Thus, parallel transmission of the same data effectively mitigates fog induced attenuation in MIMO FSO while switching on additional TxS overcomes the weak turbulence effect.

Concerning MMW signal transceivers, different approaches have been presented in this deliverable. Remote and local photonic mmW signal generation setups have been compared in an optical fronthaul based on a DML and carrier suppressed external modulation for frequency multiplying for the deployment of a 5G C-RAN fronthaul link in order to estimate the capabilities and limitations of both approaches. As theoretically predicted (i.e. 15 dB gain over 25 km fiber link), experimental EVM results in the remote generation scheme show better performance than OB2B, which is observed to increase with fiber length, whereas the local setup leads to similar performance as OB2B. Therefore, the amplitude response of the system under both configurations provides the main guideline for photonically assisted mmW C-RAN network design.

Also, with regards to MMW communication systems, a hybrid transceiver based on an MPL and a three-element antenna, operating between 24 and 28 GHz has been demonstrated with the capability of realizing beam steering in the optical domain by using the chromatic dispersion approach. It has also been shown that a PAA with only three elements can effectively steer the beam which, consequently, significantly decreases demand for radiating power to provide sufficient SNR in all cell directions. Moreover, the optically controlled steering has been tested with real data transmission at the frequency of 25 GHz, achieving an EVM as low as 5.6% with a 64-QAM modulation scheme and 20 MHz bandwidth. Experimental measurements with data transmission also confirmed theoretical assumptions about the potential usage of such an approach to be deployed in future cellular mmW frequency fronthaul networks.

Additionally, an experimental 26 GHz relay system has been presented using double RoF seamless mmW links. The proposed DSB relay system can operate with up to 20 km of SMFs deployed in the fronthaul without the need for optical amplification. Moreover, when the SSB scheme involves EDFA,

the range can be extended up to 75 km with a subsequent 5 m long FSO link while EVM is kept below the 8% for 64-QAM. Finally, we showed the use of an optoelectronic extender that can be fully integrated with a low footprint making the relay solution more compact and suitable for practical deployment.

Finally, the influence of two kinds of atmospheric conditions has been evaluated over an RS-based OCC link: the heat-induced turbulence due to random fluctuations of the refractive index of the air along the path, and the attenuation caused by the presence of fog particles in the air. Moreover, an inverse proportionality relationship between the optimum camera gain and the visibility has been identified, and also, the empirical SNR decays at a rate proportional to the optical density. This utilization of the CMOS camera's built-in amplifier opens a new possibility for OCC systems, extending the control strategy, and allowing to keep low exposure times and, thus, a high bandwidth, even in dense fog scenarios.

As a whole, for all these technical achievements, the deliverable has fulfilled the aim of providing novel solutions as advanced transceivers for wireless communications to be deployed in future generation communication networks.

5. References

- [1] Cisco, "Cisco annual internet report (2018-2023)," White paper, 2020.
- [2] ITU-R, "Report ITU-R M.2410-0. Minimum requirements related to technical performance for IMT-2020 radio interface(s)," 2017.
- [3] A. K. Majumdar, Z. Ghassemlooy, and A. A. B. Raj, "Principles and applications of free space optical communications," (in English), 2019.
- [4] Z. Htay, Z. Ghassemlooy, M. M. Abadi, A. Burton, N. Mohan, and S. Zvanovec, "Performance Analysis and Software-Defined Implementation of Real-Time MIMO FSO With Adaptive Switching in GNU Radio Platform," *IEEE Access*, vol. 9, pp. 92168-92177, 2021, doi: 10.1109/ACCESS.2021.3092968.
- [5] M. Eghbal and J. Abouei, "Performance improvement of MIMO FSO systems against destructive interference," *IET Communications*, vol. 13, no. 18, pp. 2923-2931. [Online]. Available: <https://digital-library.theiet.org/content/journals/10.1049/iet-com.2018.5027>
- [6] S. M. Moustafa, H. A. Fayed, M. H. Aly, and M. Mahmoud, "SISO and MIMO FSO based links under different weather conditions: system evaluation," *Optical and Quantum Electronics*, vol. 53, no. 12, p. 674, 2021/11/02 2021, doi: 10.1007/s11082-021-03339-3.
- [7] I. B. Djordjevic, "Adaptive Modulation and Coding for Free-Space Optical Channels," *J. Opt. Commun. Netw.*, vol. 2, no. 5, pp. 221-229, 2010/05/01 2010, doi: 10.1364/JOCN.2.000221.
- [8] M. Karimi and M. Uysal, "Novel Adaptive Transmission Algorithms for Free-Space Optical Links," *IEEE Transactions on Communications*, vol. 60, no. 12, pp. 3808-3815, 2012, doi: 10.1109/TCOMM.2012.091012.110550.
- [9] H. Nouri and M. Uysal, "Adaptive free space optical communication system with multiple apertures," in 2016 24th Signal Processing and Communication Application Conference (SIU), 16-19 May 2016 2016, pp. 937-940, doi: 10.1109/SIU.2016.7495895.
- [10] W. Hussain, H. F. Ugurdag, and M. Uysal, "Software defined VLC system: Implementation and performance evaluation," in 2015 4th International Workshop on Optical Wireless Communications (IWOW), 7-8 Sept. 2015 2015, pp. 117-121, doi: 10.1109/IWOW.2015.7342278.
- [11] O. Hiari and R. Mesleh, "A Reconfigurable SDR Transmitter Platform Architecture for Space Modulation MIMO Techniques," *IEEE Access*, vol. 5, pp. 24214-24228, 2017, doi: 10.1109/ACCESS.2017.2761859.

- [12] R. Verdecia-Peña and J. I. Alonso, "A Comparative Experimental Study of MIMO A&F and D&F Relay Nodes Using a Software-Defined Radio Platform," *Electronics*, vol. 10, no. 5, p. 570, 2021. [Online]. Available: <https://www.mdpi.com/2079-9292/10/5/570>.
- [13] L. Xiaolong, H. Weihong, H. Yousefi'zadeh, and A. Qureshi, "A case study of a MIMO SDR implementation," in *MILCOM 2008 - 2008 IEEE Military Communications Conference*, 16-19 Nov. 2008 2008, pp. 1-7, doi: 10.1109/MILCOM.2008.4753441.
- [14] H. B. Thameur and I. Dayoub, "SDR Implementation of a Real-Time Testbed for Spectrum Sensing Under MIMO Time-Selective Channels for Cognitive Radio Applications," *IEEE Sensors Letters*, vol. 5, no. 8, pp. 1-4, 2021, doi: 10.1109/LENS.2021.3095247.
- [15] S. Galih, M. Hoffmann, and T. Kaiser, "Low cost implementation for synchronization in Distributed Multi antenna using USRP/GNU-radio," in *2014 The 1st International Conference on Information Technology, Computer, and Electrical Engineering*, 8-8 Nov. 2014 2014, pp. 457-460, doi: 10.1109/ICITACEE.2014.7065791.
- [16] D. Stanko, G. Sommerkorn, A. Ihlow, and G. d. Galdo, "Enable Software-Defined Radios for Real-Time MIMO Channel Sounding," in *2021 IEEE International Instrumentation and Measurement Technology Conference (I2MTC)*, 17-20 May 2021 2021, pp. 1-5, doi: 10.1109/I2MTC50364.2021.9460077.
- [17] H. Feng, J. Wu, and X. Gong, "SOUP: Advanced SDR platform for 5G communication," in *2017 IEEE/CIC International Conference on Communications in China (ICC)*, 22-24 Oct. 2017 2017, pp. 1-5, doi: 10.1109/ICCChina.2017.8330392.
- [18] A. Costanzo, V. Loscri, and M. Biagi, "Adaptive Modulation Control for Visible Light Communication Systems," *Journal of Lightwave Technology*, vol. 39, no. 9, pp. 2780-2789, 2021, doi: 10.1109/JLT.2021.3056177.
- [19] R. Martinek, L. Danys, and R. Jaros, "Adaptive Software Defined Equalization Techniques for Indoor Visible Light Communication," *Sensors*, vol. 20, p. 1618, 03/14 2020, doi: 10.3390/s20061618.
- [20] H. Technologies. "LiFi R&D Kit." <http://www.hyperiontechs.com/lifi-rd-kit/>.
- [21] H. Boeglen, S. Joumessi-Demeffo, S. Sahuguede, P. Combeau, D. Sauveron, and A. Julien-Vergonjanne, "Optical front-ends for USRP radios," 2018.
- [22] A. Gruber, S. S. Muhammad, and E. Leitgeb, "A software defined free space optics (SD-FSO) platform based on an analog optical frontend," in *Proceedings of the 11th International Conference on Telecommunications*, 15-17 June 2011 2011, pp. 363-366.
- [23] G. Radio. "GNU Radio." <https://www.gnuradio.org/about/> (accessed 2021).
- [24] N. T. Le, M. Hossain and Y. M. Jang, "A survey of design and implementation for optical camera communication," *Signal Processing: Image Communication*, vol. 53, pp. 95-109, 2017.
- [25] V. Matus, V. Guerra, C. Jurado-Verdu, J. Rabadan and R. Perez-Jimenez, "Demonstration of a Sub-Pixel Outdoor Optical Camera Communication Link," *IEEE Latin America Transactions*, vol. 19, pp. 1798-1805, 2021.
- [26] V. Matus, V. Guerra, C. Jurado-Verdu, R. Jose and P.-J. Rafael, "Design and Implementation of an Optical Camera Communication System for Wireless Sensor Networking in Farming Fields," in *2021 IEEE International Symposium on Personal, Indoor and Mobile Radio Communications*, 2021.
- [27] V. Matus, V. Guerra, C. Jurado-Verdu, S. Zvanovec and R. Perez-Jimenez, "Wireless Sensor Networks Using Sub-Pixel Optical Camera Communications: Advances in Experimental Channel Evaluation," *Sensors*, vol. 21, 2021.
- [28] N. Saeed, S. Guo, K.-H. Park, T. Y. Al-Naffouri and M.-S. Alouini, "Optical camera communications: Survey, use cases, challenges, and future trends," *Physical Communication*, vol. 37, p. 100900, 2019.
- [29] Waterhouse, Rodney and D. Novack, "Realizing 5G: Microwave Photonics for 5G Mobile Wireless Systems," *IEEE Microwave Magazine*, vol. 16, no. 8, pp. 84-92, 2015.

- [30] W. Hong, Z. H. Jiang, C. Yu, D. Hou, H. Wang, C. Guo, Y. Hu, L. Kuai, Y. Yu, Z. Jiang, Z. Chen, J. Chen, Z. Yu, J. Zhai, N. Zhang, L. Tian, F. Wu, G. Yang, Z.-C. Hao and J. Y. Zhou, "The Role of Millimeter-Wave Technologies in 5G/6G Wireless Communications," *IEEE Journal of Microwaves*, vol. 1, no. 1, pp. 101-122, 2021.
- [31] ETSI, "5G; NR; User Equipment (UE) radio transmission and reception; Part 1: Range 1 Standalone (3GPP TS 38.101-1 V17.5.0 Release 17)," 2022.
- [32] ETSI, "5G; NR; User Equipment (UE) radio transmission and reception; Part 2: Range 2 Standalone (3GPP TS 38.101-2 version 17.5.0 Release 17)," 2021.
- [33] X. Wang, L. Kong, F. Kong, Q. Fudong, M. Xia, S. Arnon and G. Chen, "Millimeter Wave Communication: A Comprehensive Survey," *EEE Communications Surveys & Tutorials*, vol. 20, no. 3, pp. 1616-1653, 2018.
- [34] Qualcomm, "Global update on spectrum for 4G & 5G," 2020.
- [35] R. Bajracharya, R. Shrestha and H. Jung, "Future Is Unlicensed: Private 5G Unlicensed network for Connecting Industries of Future," *Sensors*, vol. 20, no. 10, 2020.
- [36] C. H. de Souza Lopes, E. Saia Lima, L. A. Melo Pereira, R. Maia Borges, A. Carvalho Ferreira, M. Abreu, W. Damascena Dias, D. H. Spadoti, L. Leonel Mendes and A. Cerqueira Sodre Junior, "Non-standalone 5G NR fiber-wireless system using FSO and fiber-optics fronthauls," *Journal of Lightwave Technology*, vol. 39, no. 2, pp. 406-417, 2021.
- [37] C. Liu, J. Wang, L. Cheng, M. Zhu and G.-K. Chang, "Key microwave-photonics technologies for next-generation cloud-based radio access networks," *Journal of Lightwave Technology*, vol. 20, no. 32, pp. 3452-3460, 2014.
- [38] C.-T. Tsai, C.-H. Lin, C.-T. Lin, Y.-C. Chi and G.-R. Lin, "60-GHz Millimeter-wave Over Fiber with Directly Modulated Dual-mode Laser Diode," *Scientific Reports*, vol. 6, no. 27919, 2016.
- [39] J. Capmany and P. Muñoz, "Integrated microwave photonics for radio access networks," *Journal of Lightwave Technology*, vol. 32, no. 16, pp. 2849-2861, 2014.
- [40] Common public radio interface: eCPRI interface specification, Common Public Radio Interface, 2019.
- [41] E. Ruggeri, A. Tsakyridis, C. Vagionas, G. Kalfas, R. M. Oldenbeuving, P. W. L. Van Dijk, C. G. H. Roeloffzen, Y. Leiba, N. Pleros and A. Miliou, "A 5G fiber wireless 4Gb/s WDM fronthaul for flexible 360 coverage in V-Band massive MIMO small cells," *Journal of Lightwave Technology*, 2020.
- [42] Intel, "Exploring 5G fronthaul network architecture intelligence splits and connectivity," White Paper, 2019.
- [43] C. Mitsolidou, C. Vagionas, A. Mesodiakaki, P. Maniotis, G. Kalfas, C. G. H. Roeloffzen, P. W. L. van Dijk, R. M. Oldenbeuving, A. Miliou and N. Pleros, "A 5G C-ROptical fronthaul architecture for hotspot areas using OFDM-based analog IFOF waveforms," *Applied Sciences*, vol. 9, no. 19, 2019.
- [44] C. Lim, A. Nirmalathas, D. Novak, R. Waterhouse and G. Yoffe, "Millimeter-wave broad-band fiber-wireless system incorporating baseband data transmission over fiber and remote LO delivery," *Journal of Lightwave Technology*, vol. 18, no. 10, pp. 1355-1363, 2000.
- [45] T. Ismail, C. P. Liu and A. J. Seeds, "Millimetre-wave gigabit/s wireless-over-fibre transmission using low cost uncooled devices with remote local oscillator delivery," *OFC/NFOEC 2007 - 2007 Conference on Optical Fiber Communication and the National Fiber Optic Engineers Conference*, pp. 1-3, 2007.
- [46] N. Argyris, G. Giannoulis, K. Kanta, N. Iliadis, C. Vagionas, S. Papaioannou, G. Kalfas, D. Apostolopoulos, C. Caillaud, H. Debregeas, N. Pleros and H. Avramopoulos, "A 5G mmWave fiber-wireless IFOF analog mobile fronthaul link with up to 24-Gb/s multiband wireless capacity," *Journal of Lightwave Technology*, vol. 37, no. 12, pp. 2883-2891, 2019.
- [47] H.-Y. Wang, Y.-C. Chi and G.-R. Lin, "Dual-mode laser diode carrier with orthogonal polarization and single-mode modulation for remote-node heterodyne MMW-RoF," *Optics Letters*, vol. 41, no. 20, pp. 4676-4679, 2016.

- [48] H. Zhang, L. Cai, S. Xie, K. Zhang, X. Wu and Z. Dong, "A novel radio-over-fiber system based on carrier suppressed frequency eightfold millimeter wave generation," *IEEE Photonics Journal*, vol. 9, no. 5, 2017.
- [49] P. Torres-Ferrera, G. Rizzelli, H. Wang, V. Ferrero and R. Gaudino, "Experimental Demonstration of 100 Gbps/ λ C-Band Direct-Detection Downstream PON Using Non-Linear and CD Compensation with 29 dB+ OPL Over 0 Km–100 Km," *Journal of Lightwave Technology*, vol. 40, no. 2, pp. 547-556, 2022
- [50] J. C. Cartledge and A. S. Karar, "100 Gb/s Intensity Modulation and Direct Detection," *Journal of Lightwave Technology*, vol. 32, no. 16, pp. 2809-2814, 2014
- [51] Y. Matsui, T. Pham, T. Sudo, G. Carey, B. Young, J. Xu, C. Cole and C. Roxlo, "28-Gbaud PAM4 and 56-Gb/s NRZ Performance Comparison Using 1310-nm Al-BH DFB Laser," *Journal of Lightwave Technology*, vol. 34, no. 11, pp. 2677-2683, 2016.
- [52] A. Delga and L. Leviandier, "Free-space optical communications with quantum cascade lasers," in *Proc. SPIE*, vol. 10926, 2019, Art. no. 1092617.
- [53] J.J. Liu et al., "Mid and long-wave infrared free-space optical communication." *International Society for Optics and Photonics.*, vol. 11133, pp. 1113302, 2019.
- [54] A.K. Majumdar et al., "Free-space laser communications: principles and advances." Springer Science & Business Media., Vol. 2. 2010.
- [55] X. Pang et al., "Direct Modulation and Free-Space Transmissions of up to 6 Gbps Multilevel Signals With a 4.65- μ m Quantum Cascade Laser at Room Temperature," *Journal of Lightwave Technology*, vol. 40, no. 8, pp. 2370-2377, 2022.
- [56] M. Joharifar et al., "High-Speed 9.6- μ m Long-Wave Infrared Free-Space Transmission With a Directly-Modulated QCL and a Fully-Passive QCD," *Journal of Lightwave Technology*, vol. 41, no. 4, pp. 1087-1094, 2023
- [57] H. Dely et al., "High bitrate data transmission in the 8-14 μ m atmospheric window using an external Stark-effect modulator with digital equalization," *Optics Express*, vol. 31, no. 5, 2023.
- [58] S. Zvanovec, J. Perez, Z. Ghassemlooy, S. Rajbhandari, and J. Libich, "Route diversity analyses for free-space optical wireless links within turbulent scenarios," *Opt. Express*, vol. 21, no. 6, pp. 7641-7650, 2013/03/25 2013, doi: 10.1364/OE.21.007641.
- [59] GNURadio. "GNURadio." <https://www.gnuradio.org/>
- [60] L. Vallejo, J. Mora, D. N. Nguyen, J. Bohata, V. Almenar, S. Zvanovec, B. Ortega, "On the 40 GHz Remote Versus Local Photonic Generation for DML-Based C-RAN Optical Fronthaul," in *Journal of Lightwave Technology*, vol. 39, no. 21, pp. 6712-6723, 1 Nov.1, 2021. [61] L. Vallejo, J. Mora and B. Ortega, "Harmonic and Intermodulation Distortion Analysis in Directly Modulated Lasers Over Local and Remote Photonicallly Generated Millimeter-Wave Signals," in *Journal of Lightwave Technology*, vol. 40, no. 15, pp. 5128-5140, 1 Aug.1, 2022, doi: 10.1109/JLT.2022.3172771.
- [62] J. Van Kerrebrouck, H. Li, S. Spiga, M. C. Amann, X. Yin, J. Bauwelinck, P. Demeester and G. Torfs, "10 Gb/s Radio-Over-Fiber at 28 GHz Carrier Frequency Link Based on 1550 nm VCSEL Chirp Enhanced Intensity Modulation after 2 km Fiber," *2018 Optical Fiber Communications Conference and Exposition (OFC)*, pp. 1-3, 2018.
- [63] Y. R. Li, B. Gao, X. Zhang, and K. Huang, "Beam management in millimeter-wave communications for 5G and beyond," *IEEE Access* 8, 13282–13293 (2020).
- [64] Z. Cao, Q. Ma, A. B. Smolders, Y. Jiao, M. J. Wale, C. W. Oh, H. Wu, and A. M. J. Koonen, "Advanced integration techniques on broadband millimeter-wave beam steering for 5G wireless networks and beyond," *IEEE J. Quantum Electron.* 52, 1–20 (2016).
- [65] V.J. Urick Jr., J. D. McKinney, and K.J. Williams, *Fundamentals of Microwave Photonics* (John Wiley & Sons, Inc, 2015).
- [66] J. Bohata, M. Komanec, J. Spáčil, P. Hazdra, T. Lonský, Z. Hradecký, and S. Zvánovec, "Experimental demonstration of a microwave photonic link using an optically phased antenna array for a millimeter wave band," *Appl. Opt.* 60, 1013-1020 (2021).

- [67] The 3rd Generation Partnership Project (3GPP), "LTE, evolved universal terrestrial radio access (EUTRA)," https://www.etsi.org/deliver/etsi_ts/136100_136199/136141/08.03.00_60/ts_136141v080300p.pdf.
- [68] J. Bohata, D. -N. Nguyen, P. T. Dat, Z. Ghassemlooy, B. Ortega and S. Zvanovec, "A Scalable 26 GHz RoF Relay System Using Optoelectronic Extender," in IEEE Photonics Technology Letters, vol. 35, no. 6, pp. 293-296, 2023.
- [69] V. Matus, E. Eso, S. R. Teli, R. Perez-Jimenez, and S. Zvanovec, "Experimentally Derived Feasibility of Optical Camera Communications under Turbulence and Fog Conditions," Sensors, vol. 20, no. 3, p. 757, 2020.
- [70] V. Matus, V. Guerra, C. Jurado-Verdu, S. R. Teli, S. Zvanovec, J. Rabadan, R. Perez-Jimenez, "Experimental Evaluation of an Analog Gain Optimization Algorithm in Optical Camera Communications," 2020 12th International Symposium on Communication Systems, Networks and Digital Signal Processing (CSNDSP), Porto, Portugal, 2020.
- [71] V. Matus, V. Guerra, S. Zvanovec, J. Rabadan, and R. Perez-Jimenez, "Sandstorm effect on experimental optical camera communication," Appl. Opt. 60, pp. 75-82, 2021.